



Erbium-based optical coherent transient correlator for the 1.5-micron communication bands
by Todd Louis Harris

A dissertation submitted in partial fulfillment of the requirements for the degree of Doctor of
Philosophy in Physics
Montana State University
© Copyright by Todd Louis Harris (2001)

Abstract:

Correlators are needed in communications, memory, and signal processing applications to perform cross-correlations for tasks such as address-header decoding for data-packet switching, spread spectrum and code division multiple access communication, associative memory, database searching, and pattern recognition. Correlators based on optical coherent transients, Fourier theory, and holography can potentially perform real-time correlations with multi-phase encoded information at gigahertz bandwidths, a capability conventional electronics lack.

The first operation of spatial-spectral holographic correlators in the 1.5- μm communication bands was demonstrated at 1536 nm using $\text{Er}^{3+}:\text{Y}_2\text{SiO}_5$ and the correlator processed multi-phase encoded optical pulses. Real-time decoding of 20-bit binary-phase-shift key encoded address-header pulses is demonstrated using stimulated photon echoes in a phase-matched crossed-beam configuration; this function is required for coherent transient optical data routing and packet switching.

Optical 30-symbol quadriphase-shift keyed (QPSK) and binary-phase-shift keyed (BPSK) codes were processed, and the results demonstrated the ability of such correlators to process QPSK codes and BPSK codes with the same apparatus. The high fidelity correlations exhibit the low sidelobe characteristics expected for the codes used.

The $4I_{15/2}$ and $4I_{13/2}$ crystal field levels of 0.005% $\text{Er}^{3+}:\text{Y}_2\text{O}_3$ were measured by absorption and laser excited fluorescence on oriented samples. Site selective fluorescence distinguished transitions of Er^{3+} in crystallographic sites of C_2 and C_3i symmetry. The paramagnetic g-tensors for ions in sites of C_2 symmetry were measured by orientation dependent Zeeman absorption spectroscopy; For the lowest crystal field level of $4I_{15/2}$ the g-tensor principal x-axis in the (100) plane is tipped $+2.06^\circ$ from [001] and principal g-values are: $g_z = 11.93$, $g_x = 1.603$, and $g_y = 4.711$. For the lowest crystal field level of $4I_{13/2}$ the g-tensor principal x-axis in the (100) plane is tipped -11.7° from [001] and principal g-values are: $g_z = 10.07$, $g_x = 1.08$, and $g_y = 4.361$. Two magnetic field orientations were identified for optimizing this material for optical coherent transient correlators: field along [111] and [110]. Fluorescence lifetimes of the lowest $4I_{13/2}$ crystal field level were measured for ions in sites of C_2 and C_3i symmetry and they were 8.51 ms and 14.62 ms, respectively.

ERBIUM-BASED OPTICAL COHERENT TRANSIENT CORRELATOR FOR THE
1.5-MICRON COMMUNICATION BANDS

by

Todd Louis Harris

A dissertation submitted in partial fulfillment
of the requirements for the degree

of

Doctor of Philosophy

in

Physics

MONTANA STATE UNIVERSITY
Bozeman, Montana

April 2001

D378
H2438

APPROVAL

of a dissertation submitted by

Todd Louis Harris

This dissertation has been read by each member of the dissertation committee and has been found to be satisfactory regarding content, English usage, format, citations, bibliographic style, and consistency, and is ready for submission to the College of Graduate Studies.

Rufus L. Cone, III

Rufus L. Cone
(Signature)

4/17/01
Date

Approved for the Department of Physics

John C. Hermanson

J. C. Hermanson
(Signature)

4-17-01
Date

Approved for the College of Graduate Studies

Bruce R. McLeod

Bruce R. McLeod
(Signature)

4-18-01
Date

STATEMENT OF PERMISSION TO USE

In presenting this dissertation in partial fulfillment of the requirements for a doctoral degree at Montana State University, I agree that the Library shall make it available to borrowers under the rules of the Library. I further agree that copying of this dissertation is allowable only for scholarly purposes, consistent with "fair use" as prescribed in the U.S. Copyright Law. Requests for extensive copying or reproduction of this dissertation should be referred to Bell & Howell Information and Learning, 300 North Zeeb Road, Ann Arbor, Michigan 48106, to whom I have granted "the exclusive right to reproduce and distribute my dissertation in and from microform along with the non-exclusive right to reproduce and distribute my abstract in any format in whole or in part."

Signature

Todd Hamer

Date

17 Apr 2001

This dissertation is dedicated to my mother,

Amy Katherine Harris.

Her continual love and support made this possible.

ACKNOWLEDGEMENTS

I want express my gratitude to my thesis advisor, Dr. Rufus Cone, for providing such extraordinary opportunities and for believing in my abilities when I did not.

Dr. Yongchen Sun has been an invaluable friend and resource; his seemingly infinite patience and ever-present sense of humor are greatly appreciated.

I thank my family and friends for their love and support.

The diverse group of graduate students, Gregory Reinemer, Tom Böttger, and Charles Thiel, in our research group and postdoctoral fellows Drs. Flurin Koenz, Nick Strickland, Alain Braud, and Geoff Pryde, visiting our research group has provided fresh and interesting perspectives on physics and life.

Nick Frankovits deserves special recognition for planting the seeds of inspiration and demonstrating the importance of perspiration.

I thank Dr. C. Michael Jefferson for providing friendship, encouragement, and entertaining discussions on all the important things in life.

Dr. Greg Francis played an immeasurable role in my success in graduate school and I thank him for the opportunity to teach with him and learn from him.

Ralph Hutcheson and Dr. Randy Equall of Scientific Materials Corp. graciously provided all the crystals used in this research.

The U.S. Air Force Office of Scientific Research (grants F49620-94-1-0465, F49620-96-1-0466, and F49620-98-0171), NSF EPSCoR, AASERT (grants F49620-97-1-041 and F49620-98-1-0283), and NASA provided financial support.

TABLE OF CONTENTS

LIST OF TABLES	viii
LIST OF FIGURES.....	ix
ABSTRACT.....	xii
1. INTRODUCTION.....	1
Correlators and Their Applications.....	1
Spectral Hole-burning and Optical Coherent Transients	3
1.5- μm Communication Bands	5
Overview of the Dissertation	6
2. BACKGROUND AND THEORY.....	9
Spectral Hole-burning Materials.....	9
Energy Levels and Spectroscopy of Er^{3+}	9
Transition Line Broadening and Material Time Scales	10
Homogeneous Broadening and Coherence Lifetime	11
Inhomogeneous Broadening.....	12
Frequency Domain Hole-burning Memory.....	13
Phenomena and Models	14
Optical Bloch Vector Model.....	14
Pulse Area and Optical Nutation.....	18
Stimulated Photon Echoes.....	19
Conditions for Linear Response.....	21
The Fourier Transform Approximation	21
Devices Based on the Fourier Transform Approximation	23
3. SPECTROSCOPY AND DYNAMICS OF $\text{Er}^{3+}:\text{Y}_2\text{O}_3$	25
Introduction and Motivation	25
Crystal Field Levels	27
Methods and Apparatus.....	31
Results and Discussion.....	34
Excited State Lifetime.....	39
Methods and Apparatus.....	39
Results and Discussion.....	41
Paramagnetic g-tensors	43
Methods and Apparatus.....	50
Results	54
Discussion	69

4. REAL-TIME ADDRESS-HEADER DECODER.....	77
Introduction	77
Application: Optical Packet Switching	78
Programming the Header Decoder	80
Decoding the Headers	81
Experimental Apparatus and Technique	83
Cross-correlation Calculations	90
Results and Discussion.....	92
Conclusions.....	95
5. CORRELATOR USING QPSK AND BPSK CODES.....	96
Introduction	96
Correlator Operation	98
Experimental Apparatus and Technique	99
Simulations.....	104
Calculations.....	105
Results and Discussion.....	107
Conclusions	110
6. SUMMARY	112
APPENDIX A	117
REFERENCES CITED	121

LIST OF TABLES

Table	Page
3.1. Crystal field levels of 0.005% Er ³⁺ :Y ₂ O ₃	39
3.2. Measured and calculated g-values for Er ³⁺ in C ₂ sites of Y ₂ O ₃	69
3.3. Two magnetic field directions that hold promise for OCT devices.....	75

LIST OF FIGURES

Figure	Page
3.1 Yttrium sesquioxide unit cell with O^{2-} sites suppressed.....	29
3.2 Rare-earth site coordination polyhedra of Y_2O_3	29
3.3. The g-tensor principal axis orientations with respect to the crystal axes.....	30
3.4. Apparatus for broadband absorption and laser induced fluorescence spectroscopies.....	33
3.5. Absorption and site selective fluorescence spectra of 0.005% $Er^{3+}:Y_2O_3$	36
3.6. Crystal field levels of ${}^4I_{15/2}$ and ${}^4I_{13/2}$ multiplets of $Er^{3+}:Y_2O_3$	38
3.7. Apparatus for measurement of ${}^4I_{13/2}$ fluorescence lifetime T_1	41
3.8. Fluorescence lifetime of Er^{3+} in C_2 sites of Y_2O_3	42
3.9. Fluorescence lifetime of Er^{3+} in C_{3i} sites of Y_2O_3	43
3.10. Graphical representation of g-tensor orientation with respect to crystal axes for the six C_2 sites in Y_2O_3 for $Er^{3+} {}^4I_{15/2};Z_1$	46
3.11. Apparatus for $Er^{3+} {}^4I_{15/2} - {}^4I_{13/2}$ Zeeman spectroscopy.....	51
3.12. Zero field absorption spectrum: C_2 site Z_1 to Y_1 transition at 6512.074 cm^{-1} . 55	
3.13. Typical Zeeman spectra of $Er^{3+}:Y_2O_3$ with $\vec{B} = 1.0\text{ T}$ along $[100]$	56
3.14. Zeeman spectra of $Er^{3+}:Y_2O_3$ vs. magnetic field strength for $\vec{B} \parallel [100]$	58
3.15. Full orientation dependent Zeeman absorption spectra for $\vec{B} = 1.0\text{ T}$ in (001)	60
3.16. Detail (* in Figure 3.15) of orientation dependent Zeeman spectra including b and c transitions with $\vec{B} = 1.0\text{ T}$ in (001) expanded for clarity.....	61

3.17. Full orientation dependent Zeeman absorption spectra for $\vec{B} = 1.0$ T in (110).....	62
3.18. Detail (* in Figure 3.17) of orientation dependent Zeeman spectra including b and c transitions with $\vec{B} = 1.0$ T in (110) expanded for clarity.....	63
3.19. g-values for ${}^4I_{15/2}:Z_1$ with field in (001).....	65
3.20. g-values for ${}^4I_{13/2}:Y_1$ with field in (001).....	65
3.21. Graphical representation of ground state ${}^4I_{15/2}:Z_1$ g-tensors can be used to visualize g-value data in Figures 3.19 and 3.23.....	66
3.22. Graphical representation of excited state ${}^4I_{13/2}:Y_1$ g-tensors can be used to visualize g-value data in Figures 3.20 and 3.24.....	66
3.23. g-values for ${}^4I_{15/2}:Z_1$ with field in (110).....	67
3.24. g-values for ${}^4I_{13/2}:Y_1$ with field in (110).....	67
3.25. Relevant energy levels and transitions for direct phonon process dephasing.	71
3.26. Relevant energy levels and transitions for spin flip-flop dephasing.	72
4.1. Optical packet switch with SSH address header decoder.....	79
4.2. Temporal snapshot of the address-header decoder programming stage.....	81
4.3. Phase matching diagrams.	81
4.4. Temporal snapshots of the address-header decoder processing stage.....	82
4.5. Schematic of the experimental apparatus used for address header decoding....	84
4.6. Block diagram of electrical apparatus used for address header decoding demonstration.....	87
4.7. Predicted echo intensity profiles assuming linear medium response and ideal excitation pulses.....	91
4.8. Results of real-time address-header decoding.....	94

5.1. Apparatus used for correlator fidelity study.....	100
5.2. Pulse sequences for correlator demonstration and laser jitter diagnosis; relative pulse timing used for this demonstration is indicated.....	102
5.3. Single-shot autocorrelation echo for QPSK code A.....	107
5.4. QPSK correlation results.....	108
5.5. BPSK correlation results.....	109

ABSTRACT

Correlators are needed in communications, memory, and signal processing applications to perform cross-correlations for tasks such as address-header decoding for data-packet switching, spread spectrum and code division multiple access communication, associative memory, database searching, and pattern recognition. Correlators based on optical coherent transients, Fourier theory, and holography can potentially perform real-time correlations with multi-phase encoded information at gigahertz bandwidths, a capability conventional electronics lack.

The first operation of spatial-spectral holographic correlators in the 1.5- μm communication bands was demonstrated at 1536 nm using $\text{Er}^{3+}:\text{Y}_2\text{SiO}_5$ and the correlator processed multi-phase encoded optical pulses. Real-time decoding of 20-bit binary-phase-shift key encoded address-header pulses is demonstrated using stimulated photon echoes in a phase-matched crossed-beam configuration; this function is required for coherent transient optical data routing and packet switching.

Optical 30-symbol quadriphase-shift keyed (QPSK) and binary-phase-shift keyed (BPSK) codes were processed, and the results demonstrated the ability of such correlators to process QPSK codes and BPSK codes with the same apparatus. The high-fidelity correlations exhibit the low sidelobe characteristics expected for the codes used.

The ${}^4\text{I}_{15/2}$ and ${}^4\text{I}_{13/2}$ crystal field levels of 0.005% $\text{Er}^{3+}:\text{Y}_2\text{O}_3$ were measured by absorption and laser excited fluorescence on oriented samples. Site selective fluorescence distinguished transitions of Er^{3+} in crystallographic sites of C_2 and C_{3i} symmetry. The paramagnetic g -tensors for ions in sites of C_2 symmetry were measured by orientation dependent Zeeman absorption spectroscopy. For the lowest crystal field level of ${}^4\text{I}_{15/2}$ the g -tensor principal x -axis in the (100) plane is tipped $+2.06^\circ$ from [001] and principal g -values are: $g_z = 11.93$, $g_x = 1.603$, and $g_y = 4.711$. For the lowest crystal field level of ${}^4\text{I}_{13/2}$ the g -tensor principal x -axis in the (100) plane is tipped -11.7° from [001] and principal g -values are: $g_z = 10.07$, $g_x = 1.08$, and $g_y = 4.361$. Two magnetic field orientations were identified for optimizing this material for optical coherent transient correlators: field along [111] and [110]. Fluorescence lifetimes of the lowest ${}^4\text{I}_{13/2}$ crystal field level were measured for ions in sites of C_2 and C_{3i} symmetry and they were 8.51 ms and 14.62 ms, respectively.

CHAPTER 1

INTRODUCTION

The primary purpose of this dissertation is the demonstration of devices that generate real-time cross-correlations of high-speed optical signals and operate in the important 1.5- μm communication bands. The frequency selective and coherence properties of spectral hole-burning (SHB) materials along with concepts and techniques from conventional holography, Fourier transforms, and optical coherent transients (OCT) are a combination ideally suited to producing real-time optical correlator devices with performance advantages over traditional computational electronics. Transparent crystalline solids activated with trivalent erbium rare-earth ions provide hole-burning media in the 1.5- μm spectral region. Correlator device performance based on and relevant properties of the Er^{3+} hole-burning materials were characterized in this dissertation.

Correlators and Their Applications

Correlators are devices that measure the similarity of two things. All observable phenomena varying in and with respect to any physical dimensions can be considered data. A correlator can measure the similarity of any two subsets of such data. Correlator devices may operate on quite different physical principles, and the data that correlators process may take quite different physical manifestations but the defining characteristic

of all correlators is the ability to perform the mathematical operation of cross-correlation.

Correlators are needed in a wide variety of memory, signal processing, and communications applications.¹ These applications include neural networks, associative memories, database searching and pattern recognition.² Particularly interesting applications in fiber and free space optical communications are data-packet address-header recognition³, spread-spectrum, and code division multiple access (CDMA) communications.⁴⁻⁷

Convolution and cross-correlation are closely related mathematical operations.⁸ The convolution $c(u)$ of two functions $f(u)$ and $g(u)$ is defined as

$c(u) = \int_{-\infty}^u f(v) g(u-v) dv$ and is written symbolically as $c(u) = f(u) * g(u)$. Sliding g

along the axis of abscissae as v is varied and integrating the product of the two functions at each overlap produces the convolution of g with f . The cross-correlation $C_c(u)$ of two

functions $f(u)$ and $g(u)$ is defined as $C_c(u) = \int_{-\infty}^u f(v) g^*(v-u) dv$ and is written

symbolically as $C_c(u) = f(u) \otimes g(u)$. Cross-correlation is similar to convolution except

that one of the original functions is complex-conjugated prior to convolution. The

special case of autocorrelation defined as $C_a(u) = \int_{-\infty}^u f(v) f^*(v-u) dv$ is obtained when

$$f(u) = g(u).$$

Fourier transforms provide a fundamental and useful method of calculating convolutions and cross-correlations of functions. In particular, the Fourier transform of the convolution of two functions is equal to the product of their Fourier transforms, so

that $c(u) = \int_{-\infty}^{\infty} F(x) G(x) e^{-ixu} dx$, where $F(x)$ and $G(x)$ are the Fourier transforms of

$f(u)$ and $g(u)$, respectively. The cross-correlation of two functions is obtained similarly, except one of the functions is complex-conjugated,

$C_c(u) = \int_{-\infty}^{\infty} F(x) G^*(x) e^{-ixu} dx$. And likewise the autocorrelation is

$C_a(u) = \int_{-\infty}^{\infty} F(x) F^*(x) e^{-ixu} dx$. A wide variety of signal processing applications¹ require

these classic operations. By exploiting the powerful Fourier transform techniques just discussed, spectral-hole burning materials are ideally suited to perform these operations on optical signals in real-time and potentially provide capabilities electronics cannot.

Spectral Hole-burning and Optical Coherent Transients

The frequency domain phenomenon, spectral hole-burning, and its time domain counterpart, optical coherent transients, can be achieved in any material with inhomogeneously broadened absorption, including atomic vapors, organic solids, and glassy or crystalline solids doped with rare earth ions. Choosing Er^{3+} as the rare-earth ion dopant provides unique capabilities in the important 1.5- μm spectral region.

Optical coherent transient phenomena are analogous to transients found in electronic and nuclear spin systems. Optical coherent transient phenomena include optical nutation, optical free induction decay, 2-pulse photon echoes, and stimulated photon echoes (SPE). Stimulated photon echoes are interesting for memory and signal processing applications when combined with ideas from conventional holography and Fourier Theory. The phase matching conditions common to conventional holography and other four-wave mixing phenomena, of which stimulated photon echoes are a transient variety, add spatial multiplexing possibilities to the memory and signal processing capabilities. Fourier Theory has provided conventional electronics and communications with powerful tools for temporal signal processing using spectral filters and in the optical domain, in combination with stimulated photon echoes, provides time domain memory and signal processing capabilities.

Three optical excitation pulses, having the correct properties outlined in Chapter 2, applied to a spectral hole-burning material will produce a fourth pulse of light called a stimulated photon echo. The input directions of the excitation pulses determine the SPE output direction. The temporal structure of the stimulated photon echo output can be crafted by temporally structuring the excitation pulses using any combination of amplitude, phase or frequency modulation as discussed in detail in Chapter 2. Spectral hole-burning materials can thus perform convolutions and cross-correlations on the modulated excitation pulses by multiplying the Fourier transforms of such pulses. Such stimulated-photon-echo-based devices are predicted to provide data processing at multi-

GHz rates with time-bandwidth products greater than 10^4 and storage densities of 10^{12} bits/cm³.

1.5- μ m Communication Bands

The demonstrated successes and future potential of fiber-optic and free-space communication networks exploit the 1.5- μ m wavelength region and make it a particularly important spectral region indeed. Much of this success is due to the Wavelength Division Multiplexing (WDM) technique in which multiple transmission channels are carried simultaneously through a single optical fiber, each channel on its own distinct optical carrier frequency, just as multiple radio transmissions are carried through the air on their own radio carrier frequency. Single channel 40 gigabits/sec (Gb/s) technology, called OC-768 in the technical literature, is in development and 10 Gb/s (OC-192) single channel transmission is widely deployed.⁹ A single-mode optical fiber with a 10 μ m core has the potential to provide total data bandwidth of 50 THz.¹⁰ Enabled by Dense Wavelength-Division Multiplexing (DWDM), the 10 terabit/sec threshold has been achieved in the laboratory over short distances¹¹ and deployed systems achieving an aggregate of 40 Gb/s (4 channels at 10 Gb/s) are state of the art.⁹ The current International Telecommunication Union (ITU) standard DWDM grid places 50 channels, each with 10 Gb/s bandwidth, at 100 GHz intervals centered on the grid anchor at 193.10 THz (1552.52 nm).

Full utilization of the impressively large single fiber bandwidth is currently not possible. Signal distortion at high bit rates and high powers due to fiber dispersion and

self- and cross-phase modulation places limitations on channel spacing and single channel bandwidth. Nonlinear crosstalk among channels owing to four-wave mixing places limitations on the number of channels, the channel spacing, and the individual channel power.

Dynamically reconfigurable networks, needed to respond to changes in bandwidth demand, require dynamic optical switching and routing. Hybrid network implementations, aimed at expanding the useable single-fiber bandwidth and increasing the variety of capabilities, employ time division multiplexing (TDM) in combination with DWDM¹² and require optical buffer memories, routers, packet address header decoders, and other switches and processors. Use of code-division multiple access (CDMA) in optical networks, requires convolvers and cross-correlators. Many opportunities for spectral hole-burning technology to provide a wide variety of new all-optical memory, switching, and processing devices exist within these efforts associated with bandwidth utilization and network management.

Overview of the Dissertation

Chapter 2 discusses the enabling properties of spectral hole-burning materials and the optical coherent transient techniques that combined to provide correlator devices. The assumptions and limitations are presented.

Chapter 3 reports a study of spectroscopic and dynamic properties of $\text{Er}^{3+}:\text{Y}_2\text{O}_3$ which is an excellent candidate for spectral hole-burning memories and processors owing to its ability to generate unusually strong stimulated photon echoes at

conveniently low external magnetic fields. The energy levels relevant for the 1.5- μm operating wavelength were determined from absorption and fluorescence spectroscopies. The excited state lifetime was measured by laser-induced fluorescence. The paramagnetic properties of the ground and excited states, which profoundly influence the dynamical behavior of the ions, were characterized with Zeeman spectroscopy as a function of magnetic field direction.

A demonstration¹³ of real-time address header decoding is presented in Chapter 4. Two distinct patterns consisting of 20-bit binary-phase-shift key encoded pulses representing data packet address headers were simultaneously stored. A phase-matched crossed beam configuration, similar to that used in conventional holographic techniques and common to four-wave mixing phenomena, was used to associate each pattern with a spatial direction. A random sequence of the two patterns was decoded and stimulated photon echoes temporally structured as the auto-correlation and cross-correlation were emitted from the crystal along the pre-programmed phase-matched directions. Address header decoding is one function required for coherent transient optical data routing, packet switching, and processing. The active medium was single-crystal $\text{Er}^{3+}:\text{Y}_2\text{SiO}_5$ operating at 1536 nm.

Chapter 5 presents a demonstration¹⁴ of time-domain optical correlations using 30-symbol quadriphase-shift (QPSK) and binary-phase-shift keyed (BPSK) codes. The codes were processed in a spatial-spectral holographic correlator with the $\text{Er}^{3+}:\text{Y}_2\text{SiO}_5$ spectral hole-burning material operating at 1536 nm. The results demonstrate the ability of spatial-spectral holographic correlators to process QPSK codes and BPSK codes with

the same apparatus. The high-fidelity correlations produced by this optical coherent transient device exhibit the low sidelobe characteristics expected for the codes used.

Chapter 6 provides summaries of the results obtained in the $\text{Er}^{3+}:\text{Y}_2\text{O}_3$ material study and in the two correlator studies and recommends future directions for the research field.

The correlator demonstrations in Chapters 4 and 5 used the $\text{Er}^{3+}:\text{Y}_2\text{SiO}_5$ hole burning material. For reference, Appendix A presents the two pulse photon echo measurements of the material coherence lifetime and stimulated photon echo measurements of spectral diffusion and stimulated echo lifetime of $\text{Er}^{3+}:\text{Y}_2\text{SiO}_5$.¹⁵

CHAPTER 2

BACKGROUND AND THEORY

This chapter describes the properties of spectral hole-burning materials and specifically the properties of Er^{3+} -doped solid-state materials. Spectral hole-burning discussion is restricted to two-level systems with population storage in a long-lived excited state. Optical coherent transient behaviors relevant to memory and signal processing devices are also described.

Spectral Hole-burning MaterialsEnergy Levels and Spectroscopy of Er^{3+}

Rare earth lanthanides (atomic numbers $N = 57$ to 71) in crystalline hosts^{16,17} are most commonly in a trivalent ionization state with a Xe-like core, closed $5s^2p^6$ outermost shells, and $4f^n$ valence electrons in the ground state. Energy levels of Er^{3+} (atomic number 68) below $\sim 80,000 \text{ cm}^{-1}$ are due to the $4f^{11}$ configuration of the valence electrons. The largest Russell-Saunders "term" in the admixture labels the levels, the total angular momentum, J , labels each "multiplet" within a term, and multiplets are $(2J+1)$ fold degenerate in the free ion. The $5s^2p^6$ wavefunctions have greater radial extent than the $4f^{11}$ wavefunctions and the latter contract toward the nucleus due to imperfect mutual screening from the nuclear potential. The $5s^2p^6$ wavefunctions shield the $4f$ electrons from static and dynamic environmental effects resulting in narrow transition linewidths. Crystal fields distort the $4f$ wavefunctions, shifting multiplets,

partially or fully lifting degeneracy within multiplets depending on the crystal field point symmetry at rare earth substituent sites, and mixing in $4f^{n-1}5d$ configuration Russell-Saunders terms. Forced electric dipole transitions are allowed among the mixed parity crystal field levels, except in site symmetries with an inversion center, and their intensities can be calculated from the Judd-Ofelt theory.^{18,19} Ions with an odd number of electrons, like Er^{3+} , exhibit Kramers degeneracy,^{16,17,20} allowing crystal fields to only partially lift the M_J degeneracy yielding up to $J + \frac{1}{2}$ crystal field levels, depending on the crystal site point symmetry thus the ${}^4I_{15/2}$ ground multiplet can be crystal-field split into at most 8 Kramers doublets and the ${}^4I_{13/2}$ first excited multiplet at $\sim 6500 \text{ cm}^{-1}$ can be crystal-field split into at most 7 Kramers doublets; the lower Zeeman component of the lowest lying ${}^4I_{15/2}$ crystal field level Z_1 serves as the ground state and the lower Zeeman component of the lowest lying ${}^4I_{13/2}$ crystal field level Y_1 serves as the excited state of the two level system for coherent transients. Magnetic dipole transitions between these states are allowed with selection rules, $\Delta J = 0, \pm 1$ and $\Delta M_J = 0, \pm 1$.

Transition Line Broadening and Material Time Scales

An ideal, isolated, two-level electronic system at zero temperature has a fundamental transition linewidth, $\Gamma_{pop}(0)$, determined by population decay from the excited state with characteristic lifetime, $T_1(0)$, given by $\Gamma_{pop}(0) = 1/2\pi T_1(0)$. Transition linewidths in real materials are always broader than this limit due to two general types of line broadening, homogeneous and inhomogeneous.

Homogeneous Broadening and Coherence Lifetime

Dynamical processes have a statistically identical influence on indistinguishable ions and cause homogeneous broadening which leaves the ions with the same dynamically perturbed transition energy. The homogeneous linewidth in Er^{3+} -doped crystals can be written as the sum of contributions from several mechanisms as

$$\Gamma_h = \frac{1}{2}\Gamma_{pop} + \Gamma_{Er-host} + \Gamma_{Er-Er} + \Gamma_{phonon}, \quad (2.1)$$

where Γ_{pop} is population decay from the excited state as before, $\Gamma_{Er-host}$ is the contribution from nuclear and electronic spin fluctuations of the host crystal, Γ_{Er-Er} is the contribution from mutual flip-flop transitions^{21,22} between Er^{3+} ions, and Γ_{phonon} represents a variety of phonon contributions. Population decay sets the ultimate lower bound on homogeneous linewidth and is almost purely radiative for decay from the lowest crystal field level of the $\text{Er}^{3+} {}^4I_{13/2}$ multiplet, with insignificant contributions from spontaneous phonon emission due to the large energy gap to lower levels (in this case $\sim 6000 \text{ cm}^{-1}$). By design the $\Gamma_{Er-host}$ contribution is minimal in this study as the two hosts, Y_2SiO_5 and Y_2O_3 , have nuclear magnetic moments of zero (^{16}O), very small values (^{89}Y), or low isotopic abundance (^{29}Si and ^{17}O).²³⁻²⁵ The phonon contribution, Γ_{phonon} , includes both direct phonon driven transitions and inelastic or Raman scattering of phonons.^{16,26-30} Room temperature homogeneous linewidths in rare-earth doped crystals are dominated by phonon contributions, and for Er^{3+} at the low temperatures used in this work, direct process transitions between Zeeman-split levels can be significant. At low temperatures, low available phonon energy and low phonon density

of states at the resonant energy generally make direct transitions between crystal field levels and such dephasing contributions insignificant. The Γ_{Er-Er} contribution includes the mutual Er-Er resonant "flip-flop" transition that is quite significant and highly dependent on choice of temperature, Er^{3+} concentration, and applied magnetic field direction and strength. Even at liquid helium temperatures, the upper Zeeman component of a weakly split Kramers doublet can be thermally populated; ions undergoing spontaneous "flip" transition from the upper to lower Zeeman component can resonantly drive another ion through a lower to upper component transition, a "flop." The resulting fluctuating magnetic field dephases yet the ion of interest by suddenly shifting its energy levels.

At liquid helium temperatures homogeneous linewidths as narrow as 10's to 100's of Hz have been observed in rare earth doped crystals.³¹⁻³³ These narrow linewidths cannot be measured directly in the frequency domain because readily available lasers have jitter-limited linewidths of a few hundred kHz; linewidths are derived from measurements of a material's coherence lifetime, T_2 , related to the homogeneous linewidth by $T_2 = 1/\pi\Gamma_h$. The coherence lifetime is measured using 2-pulse photon echo decays.^{24,34}

Inhomogeneous Broadening

Static processes within a material cause the second class of spectral line broadening known as inhomogeneous broadening. Crystal imperfections such as dislocations, impurities and other types of defects cause local stresses and strains within the crystal. The resulting distribution of local crystal fields causes a variety of perturbations on ions

at different locations within the crystal and a distribution of transition energies rendering homogeneously broadened groups of ions spectrally distinguishable. Inhomogeneous linewidths, Γ_{inh} , are highly material dependent as well and range from 100's of MHz to several THz, e.g. for Er^{3+} in silica used in erbium-doped fiber amplifiers.

Frequency Domain Hole-burning Memory

Early efforts to produce spectral hole-burning memory devices attempted to store data directly in the frequency domain.³⁵ This approach subdivided the inhomogeneous line into narrow frequency bins, each serving as a storage location in the spectral domain for a single bit. An intense "write" laser stored a digital "one" in a frequency bin by depleting the ground state population and leaving a modified inhomogeneous absorption profile; conversely, a digital "zero" was stored by not burning a hole in a particular frequency bin. Tuning the write laser across the inhomogeneous line allowed many bits to be stored in a single spatial location. In this way the entire inhomogeneous line had notches, or holes, burned in it. Spatially rastering the write laser stored multiple data sets in different spatial locations. Scanning a low intensity "read" laser through the inhomogeneous line and detecting the modified absorption read out the data.

The number of bits that could be stored in a single spatial location was fundamentally limited to $\leq \Gamma_{inh}/\Gamma_h$. However, to achieve this limit, the write laser was required to have a linewidth less than Γ_h , to dwell for a time $\tau_{burn} > 1/\Gamma_h$, and to have sufficiently low intensity to avoid power broadening. Similar requirements exist for the read laser. Frustrated by these stringent laser requirements, efforts to achieve practical

spectral hole-burning devices turned from this frequency domain approach to time-domain storage³⁶ based on the coherent transient behavior of inhomogeneously broadened materials. In contrast with frequency domain storage, the write laser in time-domain storage is rapidly modulated to burn spectrally broad, structured hole patterns representing many bits and spanning many homogeneous linewidths within the inhomogeneous profile. The remainder of this chapter discusses the theoretical tools of time-domain spectral hole burning memory and signal processing, and the optical coherent transient phenomena that form its basis.

Phenomena and Models

Optical coherent transients (OCT) are coherent responses induced in inhomogeneously broadened materials when such materials are suddenly exposed to resonant laser light, exposed to pulses of such light or when such excitations are suddenly switched off. These phenomena include optical nutation, optical free induction decay, two-pulse photon echoes, and stimulated photon echoes (SPE).³⁷⁻⁴¹ The following discussion states the important results used by this work and outlines the major theoretical approximations made, along with their implications.

Optical Bloch Vector Model

The dynamical behavior of a two-level atomic system resonantly excited by coherent laser light is mathematically analogous to a spin-one-half particle in a static magnetic field resonantly excited by a radio-frequency magnetic field.^{42,43} The spin vector formalism developed by Bloch⁴⁴ to characterize the behavior of the magnetization in

magnetic resonance experiments can be applied to optical resonance phenomena; in that case, the so-called optical Bloch vector represents the coherence and population difference induced in a two-electronic-level system. For self-consistency, the following discussion of Bloch vector formalism uses the notation of Shoemaker³⁸ throughout.

The components of the optical Bloch vector u , v , and w are defined in terms of elements of the two-level-system density matrix⁴⁵ and they have the following physical interpretation: w (defined e.g. in Equation (3-66) of Shoemaker) measures the population inversion between the ground and excited state and obtains a maximum (minimum) value of 1 (-1) when the ensemble of atoms is fully in the excited (ground) state; u and v (defined e.g. in Equation (3-65) of Shoemaker) measure, when multiplied by the ground-excited state transition dipole matrix element, the exactly in- and out-of phase components of the polarization, respectively, where phase refers to that of the driving optical field. These components can be regarded as a fictitious electric spin vector, or pseudo-dipole moment, for a homogeneously broadened ensemble of ions within an inhomogeneously broadened line.

The optical Bloch equations are the equations of motion for the optical Bloch vector, are derived from Schrödinger's Equation for an ensemble of harmonically excited two-level systems, and can be written as (e.g. Equation (3-75) and surrounding discussion of Shoemaker):

$$\begin{aligned}
\dot{u} &= (\Omega' - \omega_0) v - \frac{u}{T_2} \\
\dot{v} &= -(\Omega' - \omega_0) u + \frac{\mu_{ab} E_0 w}{\hbar} - \frac{v}{T_2} \\
\dot{w} &= -\frac{\mu_{ab} E_0 v}{\hbar} - \frac{1}{T_1} [w - (n_a - n_b)]
\end{aligned} \tag{2.2}$$

where Ω' is the laser frequency; ω_0 is the ground-excited state transition frequency which in an inhomogeneously broadened material takes a distribution of values, μ_{ab} is the ground-excited state transition dipole matrix element, E_0 is the laser electric field amplitude, and n_a and n_b are thermal equilibrium excited and ground state populations, respectively. Customarily, relaxation terms are added phenomenologically using $\frac{1}{T_2}$ as

the coherence decay rate and $\frac{1}{T_1}$ as the population decay rate;⁴⁴ the former only contributes to decay of u and v , and the latter only contributes to decay of w .

The primary approximation made in deriving the optical Bloch equations is that the optical radiation field is very nearly monochromatic and almost exactly on resonance with one transition frequency of the atom under consideration.³⁷ This approximation immediately implies a two-level system³⁷ and is an excellent approximation for Er^{3+} -doped crystalline solids at low temperatures; indeed, as discussed previously and illustrated by the work presented in Chapter 3, one strives to find a medium with suitable host lattice properties and Er^{3+} dopant concentration, and temperature and external magnetic field conditions to minimize the effects that cause deviation from pure two-level-system behavior.

The on-resonance assumption makes possible an additional approximation known as the Rotating Wave Approximation (RWA). The RWA is valid if the rate at which population is driven from the ground to excited state is very small compared to the optical transition frequency;³⁹ for the demonstrations presented in Chapters 4 and 5 the RWA is justified because the rate at which population was driven from ground to excited state never exceeded $\sim 10^7$ Hz and the optical transition frequency was $\sim 10^{14}$ Hz. In the derivation of the optical Bloch equations the RWA neglects terms that oscillate at twice the optical frequency; the rationale is that rapid gyrations of the Bloch Vector at twice the laser frequency tend to average out on the time scales of interest. In the work presented in Chapters 4 and 5 the time scales of interest were $> 10^{-8}$ seconds and the optical period was $< 10^{-14}$ seconds which provides additional justification for use of the RWA in that work. The RWA neglects effects that, in principle at least, are observable, these include sum frequency generation³⁹ and a small shift of the resonant frequency which in magnetic resonance is called the Bloch-Siegert shift and is negligible in optical experiments.^{37,38}

A graphical interpretation of solutions of the optical Bloch equations is called the vector model³⁷⁻⁴⁰ and was developed by Feynman, Vernon, and Hellwarth.⁴² This model is useful for visualizing and predicting material polarization state and its evolution under a variety of simple but important excitation schemes; the language of the vector model is used below in discussion of the optical coherent transient phenomena relevant to this work. In a wide variety of excitation schemes that are too complicated for simple visualization, numerical simulation techniques using this Bloch formalism can predict

two-level-system response; indeed, numerical simulation of the optical Bloch equations is used in Chapter 5 to model complicated correlator performance.

Pulse Area and Optical Nutation

It is useful to characterize laser pulses by their so-called “area,” which is defined, (e.g. in Shoemaker Equation (3-128)):

$$\begin{aligned}\theta &= \kappa \int_{-\infty}^{\infty} E_0(t) dt \\ &= \kappa E_0 \tau = \Omega \tau \quad \text{for rectangular pulses}\end{aligned}\tag{2.3}$$

where $\kappa = \frac{\mu_{ab}}{\hbar}$, $E_0(t)$ is the amplitude envelope of the laser electric field, τ is the pulse duration, and Ω is the Rabi frequency on resonance. The pulse area measures the effect a laser pulse has on the two-level system and is usually given in units of π radians to denote the angle through which a pulse rotates the optical Bloch vector. Estimating pulse area is important for comparison of experiment with theory but is inexact in practice as the laser electric field E_0 always has a non-uniform spatial distribution governed by diffraction and absorption; Gaussian profiles across the beam and laser absorption throughout the crystal cause a spatial distribution of pulse areas. Also, inhomogeneous broadening of the absorbing medium takes atoms off of exact resonance with the laser causing a spectral distribution of pulse areas. When used to estimate pulse areas, optical nutation accounts for some of these effects and within certain limits conveniently allows others to be neglected as described below.

Optical nutation^{41,46,47} describes the transient effect that occurs when an ensemble of atoms is suddenly exposed to intense resonant laser light and is analogous to the spin

nutation phenomenon in magnetic resonance.⁴⁵ Ions in the ensemble undergo alternate absorption and emission of light as they are driven coherently between the ground and excited states by the laser field.⁴¹ In nutation experiments the total detected signal is the sum of the transmitted portion of the incident laser field and the field emitted by the polarization induced in the sample; in an experiment using a laser with a Gaussian profile across the beam, a crystal with low total absorption $\alpha L \leq 1$, (where α is the Beer-Lambert Law absorption coefficient and L is the length of the medium along the direction of laser propagation) and a single transition dipole moment⁴⁸ the nutation signal behaves approximately as:

$$S \propto \frac{\Omega^2 J_1(\Omega t)}{\Omega t} \quad (2.4)$$

where J_1 is the first order Bessel function.³⁸ The first maximum of the expression in Equation 2.4 above is at $\theta = \Omega t \cong 1.65\pi$. This approximation is valid if rise time τ_r of

the excitation pulse and material coherence lifetime T_2 satisfy $\tau_r \ll \frac{1.65\pi}{\Omega} \ll T_2$; in the

work presented in Chapter 5, where $\tau_r \cong 35$ ns, $\frac{1.65\pi}{\Omega} \geq 100$ ns, and $T_2 \cong 70$ μ s, nutation

experiments and this approximation were used to estimate pulse areas for comparison of correlator performance with simulations.

Stimulated Photon Echoes

The pulse sequence required for generating a stimulated photon echo is described below. The absorbing medium is assumed to start in equilibrium with a fully populated ground state and zero population in the excited state. At time $t = 0$ a pulse is applied on

resonance with the transition. This pulse has duration $t_1 \ll T_2$ such that it burns holes over many homogeneous packets, though not evenly, in the inhomogeneous line. In the low pulse area limit, the Fourier transform of this pulse is burned into the absorption line and the ions are placed in a superposition of the ground and excited states. The optical electric field amplitude and phases of the spectral components of the optical electric field are recorded (in resonant homogeneous packets) in the inhomogeneous line. Amplitude is recorded as hole depth, the relative fraction of ions in excited versus ground state. Optical phase is recorded as phase of ensemble oscillation in their superposition states. A macroscopic polarization is created leaving the ions oscillating coherently after the pulse, and this coherence decays with the material coherence lifetime T_2 . The inhomogeneous distribution of natural oscillation frequencies of the various ions causes them to lose coherence with one another over time, but population difference persists for a time scale of T_1 .

A second pulse applied to the medium at time $t = t_2 < T_2$, while the coherence created by pulse one persists, interferes with the first pulse. The second pulse can transfer the ions from the superposition states created by pulse one, and tends to convert the associated coherences into excited state and ground state population gratings. These population gratings can be thought of as filters, spectrally shaped by the product of the Fourier transforms of the two pulses in the low pulse area limit, and they persist for the material upper state lifetime T_1 . The temporal interference of pulses in the medium is the motivation for referring to this technique as spectral holography and the material phase

memory allows this interference to occur even when the pulses are not present simultaneously in the medium.

A third pulse applied to the population gratings at $t = t_3 < T_1$ converts the gratings back into coherences, placing the ions again in superposition states; the coherence increases in time as the ions rephase, re-establishing an oscillating macroscopic polarization in the medium. The medium emits another pulse called a stimulated photon echo at time $t = t_3 + (t_2 - t_1) = t_3 + \tau_{21}$.

Conditions for Linear Response

In general, the stimulated echo intensity depends on the three input pulse intensities, I_k , and areas, θ_k , with $k = 1, 2, 3$ through:³⁹

$$I_s \propto I_1 I_2 I_3 \left(\sin(\theta_1) \sin(\theta_2) \sin(\theta_3) \right)^2. \quad (2.5)$$

Pulses with areas $< \frac{\pi}{2}$ are necessary if linear response is desired since the Fourier transforms of the pulses are not faithfully recorded or reproduced by the medium for $\frac{\pi}{2}$ -pulses. Most practical devices have the mutually incompatible requirements that output signals be maximally intense and minimally distorted which suggests that a device-specific and application-specific tradeoff must always be found.

The Fourier Transform Approximation

Proposals^{36,49-52} that the stimulated photon echo could be used to perform cross-correlation and convolution operations transformed the subject from one of scientific curiosity to one of technological application; this is readily seen when the stimulated photon echo electric field E_s is expressed as:

$$E_S(t) \propto \int_{-\infty}^{\infty} E_1^*(\omega) E_2(\omega) E_3(\omega) e^{-i\omega(t-(t_3+\tau_{21}))} d\omega \quad (2.6)$$

where $E_k(\omega)$ is the Fourier transform of the electric field envelope of the k^{th} pulse, ω is the optical frequency, t_3 is the arrival time of pulse three, and τ_{21} is the delay between pulses one and two. The limits of validity for this approximation are that the excitation pulse areas are low, $\theta < 0.3\pi$, so that the material responds linearly to the Fourier Transform of the pulse, that the pulse bandwidths are well within the inhomogeneous linewidth, that the delay between pulses one and two, τ_{21} , is shorter than the coherence lifetime T_2 , and that pulse three is applied at a time, t_3 , within the upper state lifetime, T_1 .

Babbitt⁵² provided further justification for the Fourier Transform Approximation (FTA) above by demonstrating through a density matrix calculation that pulses of low area generate response in the material proportional to the pulse Fourier Transform. Later the FTA was experimentally verified.⁵³

The primary result of the FTA is prediction of the stimulated photon echo temporal structure, arrival time, and output direction. In the FTA the temporal structure of the stimulated photon echo is the cross-correlation of pulse 1 with the convolution of pulses 2 and 3. The SPE arrival time is approximated as:

$$t_s = t_3 + (t_2 - t_1), \quad (2.7)$$

but depends in general on the intensity, structure, duration, and propagation effects of the excitation pulses.⁵⁴ Finally, if the excitation pulses can be regarded as plane waves, the phase matching conditions:

$$\vec{k}_s = \vec{k}_3 + (\vec{k}_2 - \vec{k}_1), \quad (2.8)$$

are obtained. The special case of $\vec{k}_1 = \vec{k}_3$ which sets $\vec{k}_s = \vec{k}_2$ is useful for spatially separating the intense third excitation pulse from the weak SPE output signal to aid in detection of the latter. This scheme is also utilized in Chapter 4 to spatially discriminate a number of output signals from many spatial-spectral gratings along corresponding \vec{k}_s directions programmed by choice of \vec{k}_2 directions.

Devices Based on the Fourier Transform Approximation

The FTA can be used to craft a wide variety of devices^{52,54} by choice of input pulse shape, timing, and propagation direction. For device purposes, the input pulses fall into two categories, reference pulses and temporally structured waveforms. The temporally structured waveforms typically contain data that is to be stored or processed by the device. The reference pulse, whose name is taken from conventional holography to imply a function analogous to the reference beam, contains no information but is used as a “write” pulse and interfered with a temporally structured waveform to store a spatial-spectral grating or as a “read” pulse to generate a stimulated photon echo from a stored grating. The reference pulse timing and input direction can be used to control the stimulated photon echo emission time and output direction. The reference pulse is

required to have constant spectral amplitude over the bandwidth of the temporally structured waveforms and can be of arbitrarily large area without sacrificing linear response. This is typically accomplished, and is always the case in this work, by making it temporally brief compared with any structure in the temporally structured waveforms, although chirped reference pulses of longer duration have been proposed and demonstrated.⁵⁴

The most important processor device for this work is the correlator. If pulse 2 is a spectrally flat over the bandwidth of pulses 1 and 3, the FTA reduces to,

$$E_s(t) \propto \int_{-\infty}^{\infty} E_1^*(\omega) E_3(\omega) e^{-i\omega(t-(t_3+\tau_{21}))} d\omega, \quad (2.9)$$

the cross-correlation between pulses 1 and 3, which are arbitrary temporally structured waveforms. The special case of auto-correlation is obtained when pulses 1 and 3 are identical. The temporal length of the pattern in pulse 1 is set by T_2 and the upper bound on the processing for pulse 3 is set by T_1 . The correlator demonstrations of Chapters 4 and 5 are based upon this reduced version of the FTA.

When pulse 1 is chosen to be a reference pulse and pulses 2 and 3 are temporally structured, the FTA reduces to

$$E_s(t) \propto \int_{-\infty}^{\infty} E_2(\omega) E_3(\omega) e^{-i\omega(t-(t_3+\tau_{21}))} d\omega, \quad (2.10)$$

the convolution of pulses 2 and 3. The convolution process is fundamental as described in Chapter 1 and has interesting communication applications in conjunction with cross-correlation as discussed in Chapter 6.

CHAPTER 3

SPECTROSCOPY AND DYNAMICS OF $\text{Er}^{3+}:\text{Y}_2\text{O}_3$ Introduction and Motivation

The Er^{3+} ion is of considerable interest for optical signal processing and memories using OCT techniques, because the ${}^4\text{I}_{15/2}$ to ${}^4\text{I}_{13/2}$ transitions can provide a device in the 1.5 μm fiber-optic communication bands, where this same transition is used in Erbium-doped Fiber Amplifiers (EDFA) to provide signal gain. Trivalent erbium in YAG, glass and other hosts is also used as a solid-state laser material providing emission near 3 μm , utilizing a different set of energy levels from those given above. A study of the spectroscopy and dynamics of Er^{3+} in the Y_2O_3 host is presented here; this system is particularly interesting for OCT devices.

The coherence lifetime T_2 determines two-pulse photon echo lifetime, limits stored-pattern temporal duration in an OCT correlator, and through its spectral domain counterpart, homogeneous linewidth Γ_h , limits spectral resolution of any OCT device; excited state lifetime sets an upper bound on coherence lifetime. Dynamical behavior of the environment surrounding the correlator ions reduces coherence lifetime through the mechanisms of phonon scattering and magnetic spin flips. Operating at low temperature reduces the significance of direct phonon transitions; phonons of the resonant frequency become unavailable to drive direct transitions as the density of states at the resonant frequency and the maximum available phonon energy become reduced. Nuclear and

electronic spin flips of host crystal ions contribute to dephasing as well. By design, the Y_2O_3 host^{23,24} lattice contributes minimally to the fluctuating local field; the constituent nuclear magnetic moments are either zero as in the case of ^{16}O , very small as in the case of ^{89}Y with a moment $-0.14 \mu_N$ (the nuclear magneton, $\mu_N = \frac{e\hbar}{2m_p}$), or of low enough isotopic abundance as not to be of consequence as in the case of 0.04% abundant ^{17}O with a moment of $-1.89 \mu_N$. Erbium ions substitute with equal probability into ten spectroscopically distinct Y^{3+} sites in the Y_2O_3 host as discussed on the next page; an OCT device is thereby restricted to be comprised of a fraction of the total Er^{3+} ions, called "device ions" ("A" ions in the terminology of Mims)^{21,22} and leaves a fraction of Er^{3+} ions unused for the device, called "environment ions" ("B" ions in the terminology of Mims).^{21,22} The primary⁵⁵ low magnetic field, low temperature dephasing mechanisms in this system are device ion electronic spin flips driven by direct process phonon transitions²⁶⁻³⁰ and environment ion mutual "flip-flop" transitions which dephase device ions through the resulting fluctuating magnetic field.^{21,22} Device ions can dephase other device ions through the flip-flop process and in this context can be regarded as environment ions as well.

The crystal field levels used for an OCT device and those that influence its performance were located by absorption and fluorescence spectroscopy of transitions between the $\text{Er}^{3+} {}^4\text{I}_{15/2}$ and ${}^4\text{I}_{13/2}$ multiplets. Excited state lifetime was measured by laser-excited fluorescence decay. Device ion and environment ion paramagnetic g-tensors, which guide choice of external magnetic field direction and strength to optimize

coherence lifetime, were measured by orientation dependent Zeeman spectroscopy. This information can be used to optimize $\text{Er}^{3+}:\text{Y}_2\text{O}_3$ for OCT devices.

Crystal Field Levels

Crystal fields modify Er^{3+} free-ion energy levels and spectroscopy as discussed in Chapter 2. Trivalent erbium exhibits Kramers degeneracy^{16,17,20} as it is an odd electron ion, with the $4f^{11}$ valence electrons inside the $5s^2p^6$ closed shells. The result of Kramers degeneracy is that the Stark effect can only lift half of the $(2J+1)$ fold degeneracy of a J -multiplet and only the Zeeman effect can lift the remaining two-fold degeneracy. A crystal field, depending on its symmetry, can split the 16-fold degenerate $^4I_{15/2}$ ground and 14-fold degenerate $^4I_{13/2}$ first excited multiplets of Er^{3+} into 8 and 7 doubly degenerate crystal field levels, respectively.

The yttrium sesquioxide host crystal is cubic and belongs to the T_h ⁷ space group, with 16 formula units per unit cell.⁵⁶ Triply ionized rare-earth dopants can substitute into the Y^{3+} sites without charge compensation. Of the 32 such rare earth sites in the unit cell, 24 are of C_2 point symmetry and 8 are of C_{3i} point symmetry.⁵⁶ Using electron paramagnetic resonance (EPR) rare earth ions were first observed to substitute into both the C_2 and C_{3i} Y^{3+} sites with equal probability with Yb^{3+} as the dopant ion.⁵⁷ Further EPR studies showed that Er^{3+} also substituted into both C_2 and C_{3i} Y^{3+} sites.^{58,59}

The Y_2O_3 unit cell is depicted in Figure 3.1⁶⁰ with the O^{2-} sites suppressed; circles represent the two types of rare-earth sites with open circles for C_2 sites and solid circles for C_{3i} sites. The C_{3i} sites, numbered 1-4, are orientationally inequivalent, with their

local C_{3i} symmetry axes along the $[111]$, $[11\bar{1}]$, $[1\bar{1}1]$, and $[\bar{1}11]$ crystal axes, respectively. The C_{3i} site nearest neighbor O^{2-} sites define the vertices of the polyhedron centered on the ion site labeled 1 and are shown removed from the unit cell and enlarged in Figure 3.2.⁵⁸ The C_2 sites, numbered 5-10, are orientationally inequivalent, with the C_2 axes for 5 and 6 along $[100]$, 7 and 8 along $[010]$, and 9 and 10 along $[001]$. The C_2 site nearest neighbor O^{2-} sites define the vertices of the polyhedron centered on the ion site labeled 5 and are shown removed from the unit cell and enlarged in Figure 3.2.⁵⁸ In sites of C_2 symmetry the crystal only imposes the C_2 symmetry axis, by convention the z-axis in the context of the Er^{3+} paramagnetic g-tensors; the principal x and y axes of the g-tensor can be tipped at a different angle α with respect to the crystallographic axes for each crystal field energy level as shown in Figure 3.3.⁵⁹ Following in this chapter is a detailed discussion of the g-tensors, their importance to the dynamical behavior of $Er^{3+}:Y_2O_3$, and their measurement.

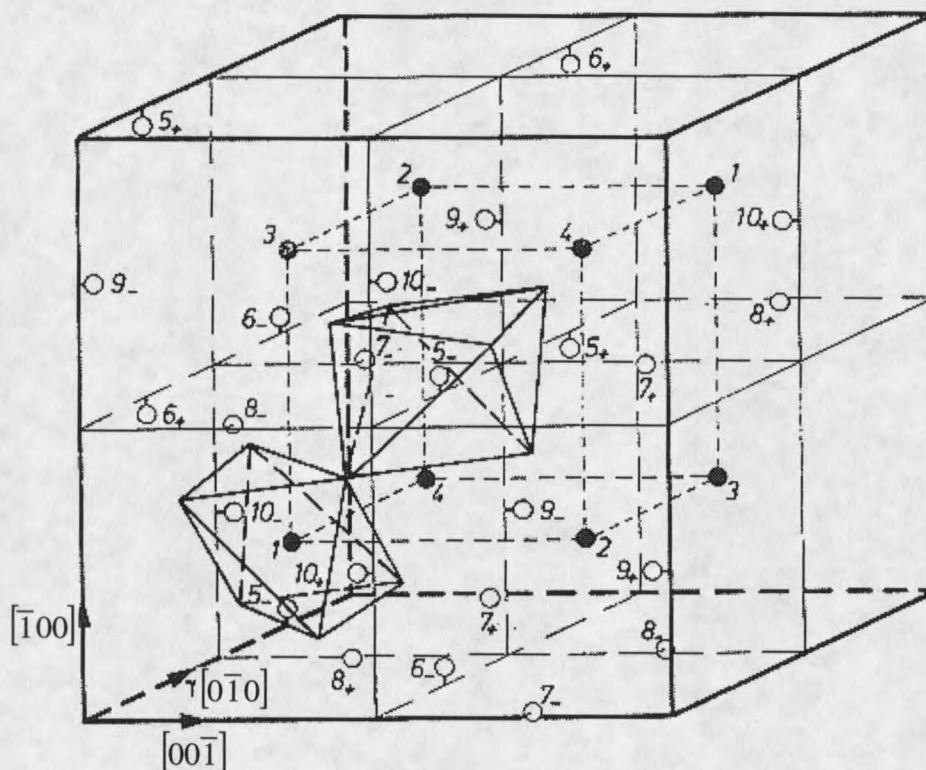


Figure 3.1 Yttrium sesquioxide unit cell with O^{2-} sites suppressed. Sites with C_{3i} symmetry (\bullet) are labeled 1-4, and sites with C_2 symmetry (\circ) are labeled 5-10, (Reproduced from reference 60).

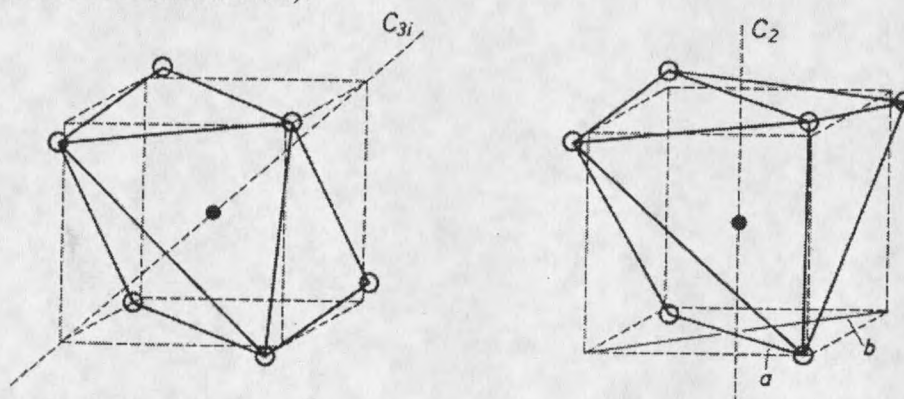


Figure 3.2 Rare-earth site coordination polyhedra of Y_2O_3 . Nearest neighbor O^{2-} sites (\circ) are vertices and C_2 and C_{3i} sites (\bullet) are at centers of cubes. (Reproduced from reference 58).

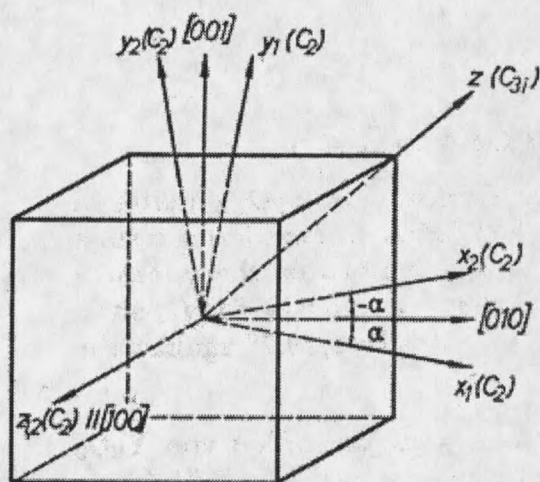


Figure 3.3. The g-tensor principal axis orientations with respect to the crystal axes. (Reproduced from reference 59).

The first spectroscopic studies of $\text{Er}^{3+}:\text{Y}_2\text{O}_3$, located the two lowest crystal field levels of the $^4\text{I}_{15/2}$ multiplet at 0 and 38.9 cm^{-1} using fluorescence from the $^4\text{S}_{3/2}$ multiplet; the $^4\text{F}_{9/2}$ multiplet at $15,000 \text{ cm}^{-1}$ and other higher multiplets but no lower multiplets were determined with absorption spectroscopy.⁶¹ These transitions were all attributed to forced electric dipole transitions within ions in C_2 sites as the C_{3i} site inversion center forbids electric dipole transitions.^{16,17} Fluorescence from the $^4\text{S}_{3/2}$ multiplet located all seven $^4\text{I}_{13/2}$ and all eight $^4\text{I}_{15/2}$ crystal field levels for C_2 ions; absorption and fluorescence spectroscopies located all other crystal field levels up to $43,000 \text{ cm}^{-1}$; magnetic dipole allowed $^4\text{I}_{15/2} \leftrightarrow ^4\text{I}_{13/2}$ transitions within C_{3i} ions were not observed since experimental facilities for direct $1.5 \mu\text{m}$ spectral region absorption were not available.⁶² Crystal field analyses for ions in C_2 sites were performed and compared

with experiment; the average deviation between the 65 observed and predicted levels was 11 cm^{-1} .⁶³

In the present work, lamp absorption experiments and site-selective fluorescence excitation experiments using $1.5 \text{ }\mu\text{m}$ diode lasers, located the crystal field levels of the ${}^4\text{I}_{15/2}$ and ${}^4\text{I}_{13/2}$ multiplets for the ions in both C_2 and C_{3i} sites in $0.005\% \text{ Er}^{3+}:\text{Y}_2\text{O}_3$.⁶⁴ Energy levels of the higher multiplets are of no consequence for this study as the next multiplet ${}^4\text{I}_{11/2}$ is 3500 cm^{-1} above the ${}^4\text{I}_{13/2}$.

Methods and Apparatus

Scientific Materials Corporation of Bozeman, Montana provided several pieces of $0.005\% \text{ Er}^{3+}:\text{Y}_2\text{O}_3$ grown by their proprietary top-seeded-solution method.⁶⁵ One such piece was oriented by Laue X-ray diffraction. The crystal was cut, ground, and polished to produce two opposing faces normal to $[111]$, two opposing faces normal to $[1\bar{1}0]$, and a single face normal to $[11\bar{2}]$. The remaining side, normal to $[11\bar{2}]$, was left as received. The crystal dimensions along $[111]$ and $[1\bar{1}0]$ and $[11\bar{2}]$ were 3.47, 6.55, and $\sim 5 \text{ mm}$, respectively.

The absorption and fluorescence spectroscopy apparatus is shown schematically in Figure 3.4. The crystal was immersed in liquid helium at 1.5 K in an Oxford Instruments Optistat-Bath cryostat (CRYO) which had two opposing pairs of windows (W) for optical access. The filament of a tungsten halogen lamp (LAMP) was imaged inside the crystal and propagation along the thickest dimension of the sample yielded maximum available absorption. The transmitted light was focused on the entrance slits of a SPEX

Model 1000M monochromator (SPEX). The monochromator gratings had 600 grooves/mm, were blazed at 1.5 μm , and provided 0.8 nm/mm reciprocal dispersion. The entrance and exit slits were set to 100 μm width, and the monochromator was scanned over the spectral region where absorption lines were expected from previous studies.⁶³ A colored glass bandpass filter (FIL) with 0.94 transmittance between 950 and 2900 nm was placed between the lamp and the cryostat to eliminate visible light that could pass through the monochromator at the same grating orientation as the 1.5- μm absorption spectrum but in a higher grating order. The monochromator exit slit was imaged onto either a Hamamatsu NIR PMT Model R5509-72 or a liquid nitrogen cooled Advanced Detector Corporation Model 403L Germanium detector (PMT/Ge). A Tektronix TDS 520D oscilloscope (SCOPE) monitored the output from either detector. An 80486-based micro-computer, not shown in Figure 3.4, recorded the spectra by collecting the generated photocurrent from the photodetector at each monochromator grating position.

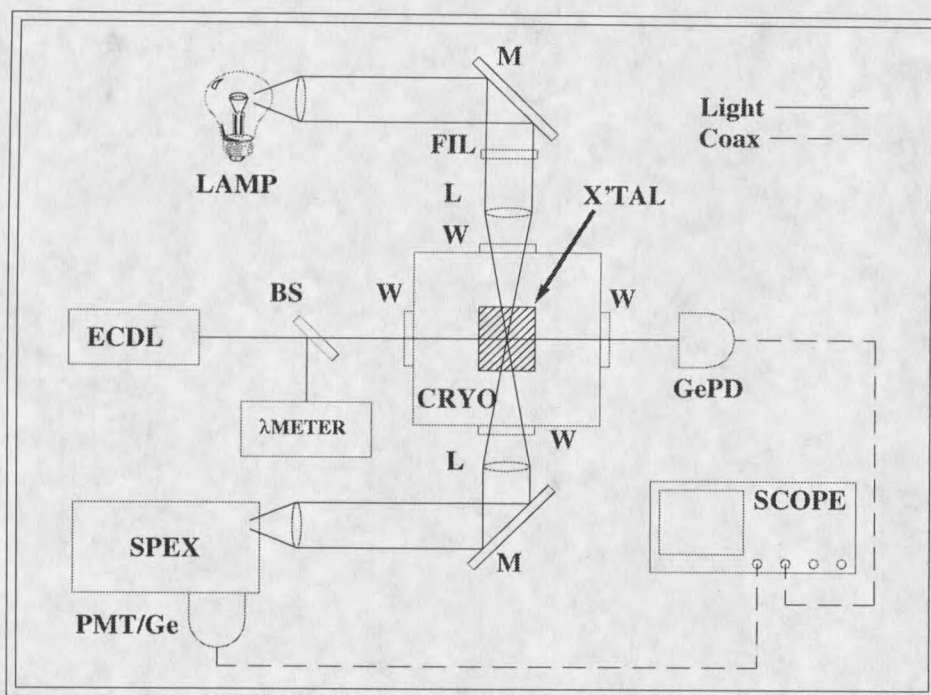


Figure 3.4. Apparatus for broadband absorption and laser induced fluorescence spectroscopies.

A Littman-Metcalf configuration external cavity diode laser (ECDL)⁶⁶⁻⁷¹ excited fluorescence, in turn, from each of the absorption lines. The laser was focused through the cryostat and through the crystal along the $[1\bar{1}0]$ direction; the fluorescence exiting the cryostat at 90° along $[111]$ was collected and focused into the monochromator. A Burleigh WA-1500 wavemeter (λ METER) monitored the laser wavelength and individual crystal absorption lines could be observed by scanning the laser over a ≤ 46 GHz range and observing the transmission on a New Focus 2033 Large Area Germanium photodiode (GePD). To detect fluorescence, the monochromator was scanned and the computer recorded the spectra as before.

Results and Discussion

Direct excitation and observation of absorption and fluorescence in the 1.5 μm region using the apparatus and techniques described above allowed more detailed characterization of $\text{Er}^{3+}:\text{Y}_2\text{O}_3$ than previously possible. Previous measurements and crystal field analyses of the energy levels of ions in C_2 sites^{62,63,72} served as an initial guide for assignment of a particular site to a set of absorption lines that produced identical fluorescence spectra. Also, ions in C_2 sites were expected to have larger absorption line intensities than those of ions in C_{3i} sites; there are three times as many C_2 sites as C_{3i} sites and forced electric dipole transitions are allowed for the former but not for the latter due to its inversion center. These observations and arguments aided interpretation of the spectra.

The low temperature insured that only the lowest crystal field level of the ground multiplet would be populated, and the spectral region observed insured that absorption would terminate in a level of the first excited multiplet. In general, ions in the two crystallographic sites have different crystal field levels and spectra. Absorption spectroscopy alone was not sufficient to distinguish the two interspersed sets of absorption lines belonging to ions in C_2 and C_{3i} sites. But, for each site, fluorescence spectra from each of the higher $^4\text{I}_{13/2}$ levels (labeled Y_2 to Y_7) should have identical features to fluorescence spectra from the lowest $^4\text{I}_{13/2}$ level (Y_1), and all measured the position of the $^4\text{I}_{15/2}$ levels (Z_1 up to Z_8). Ions pumped from the $^4\text{I}_{15/2}:\text{Z}_1$ to the $^4\text{I}_{13/2}:\text{Y}_2$ and higher $^4\text{I}_{13/2}$ levels rapidly and non-radiatively relaxed to the $^4\text{I}_{13/2}:\text{Y}_1$ level from which fluorescence to all levels of the ground multiplet simultaneously occurred. Two

distinct fluorescence spectra were obtained from individually pumping each of the absorption lines and suggested that each of the two groups of absorption lines belonged to ions in either the C_2 or C_{3i} sites.

Absorption and fluorescence spectra obtained by the methods described above are shown in Figure 3.5. The absorption spectra contained all absorption lines expected for transitions to the $^4I_{13/2}$ crystal field levels of ions in C_2 sites from previous studies⁶² thus confirming and extending the results of the earlier visible fluorescence experiment. Above the absorption spectrum is a comb of seven vertical bars indicating the C_2 site absorption lines. These absorption lines consistently yielded fluorescence spectra like that of the bottom trace in Figure 3.5 which agree well with the $^4I_{15/2}$ C_2 crystal field levels cited in previous studies.⁶² The feature at 6000 cm^{-1} is similar to that obtained previously⁶² and was previously believed⁶³ to be two lines separated by 20 cm^{-1} and corresponding to the Z_7 and Z_8 crystal field levels of the $^4I_{15/2}$ multiplet as eight crystal field levels are expected for the $^4I_{15/2}$ multiplet in C_2 symmetry. Interspersed with the C_2 absorption lines were additional absorption lines, indicated above the absorption spectrum with a comb of four vertical bars and labeled as C_{3i} site absorption lines and were not consistent with known absorption by C_2 ions; all previous observations of absorption by Er^{3+} in C_{3i} sites were on stoichiometric Er_2O_3 .⁷³ The fluorescence spectra from the remaining, interspersed, absorption lines yielded a consistent fluorescence line pattern, the middle trace in Figure 3.5, distinct from that expected for C_2 ion crystal field levels. The new absorption and fluorescence lines were attributed to the ions in C_{3i} sites, and G. Reinemer's Zeeman experiments⁶⁴ confirmed this hypothesis.

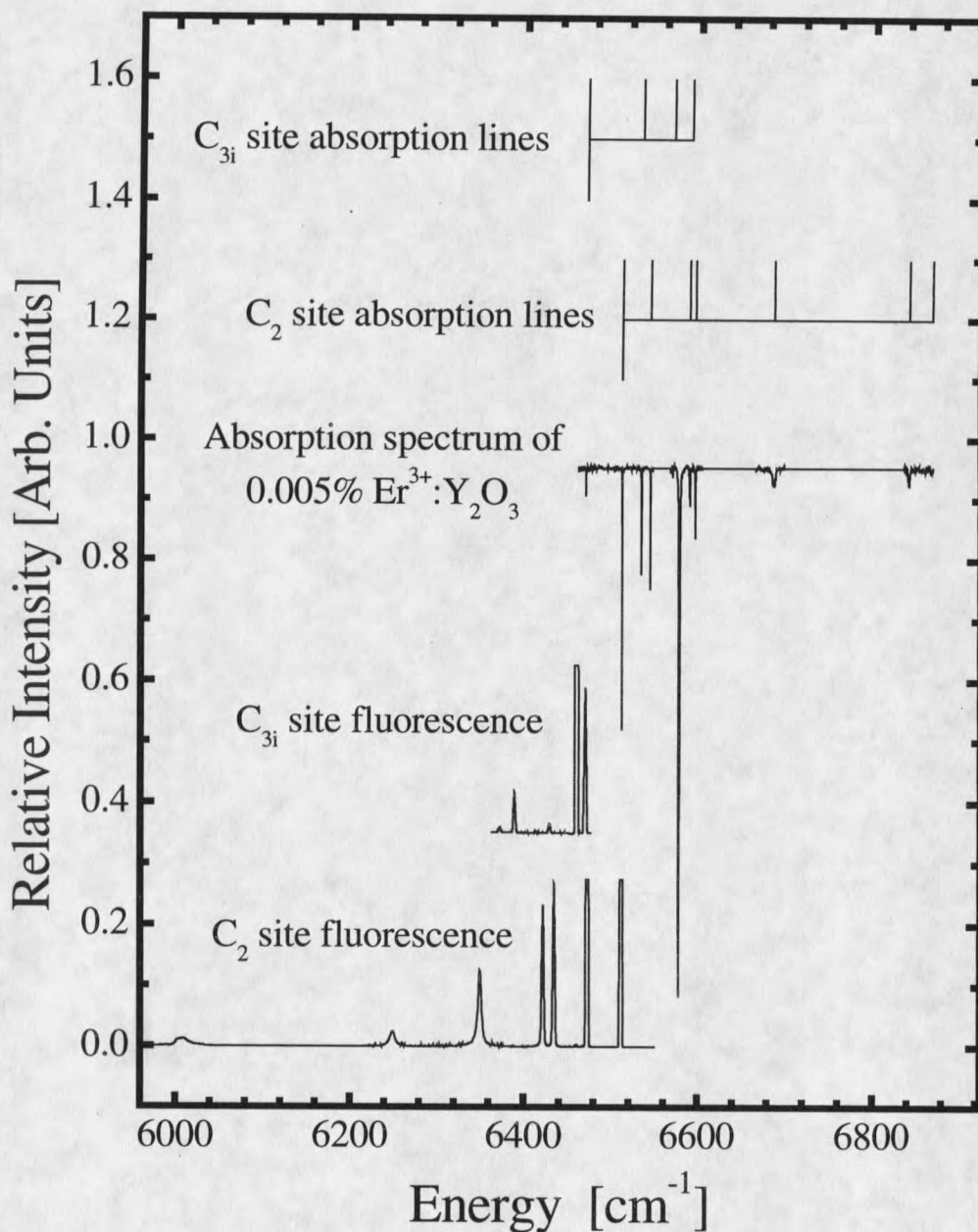


Figure 3.5. Absorption and site selective fluorescence spectra of 0.005% $\text{Er}^{3+}:\text{Y}_2\text{O}_3$. At top of figure, two combs of vertical bars denote absorption lines assigned to ions in C_{3i} sites (upper comb) and to ions in C_2 sites (lower comb) from absorption spectrum immediately below them. Site selective fluorescence spectra generated by pumping absorption lines; upper and lower traces are fluorescence from absorption lines assigned to ions in C_{3i} (Reference 64) and C_2 sites.

The ${}^4I_{15/2}$ and ${}^4I_{13/2}$ crystal field levels determined by this study for the C_2 and C_{3i} ions are presented in Figure 3.6 and Table 3.1. The left three columns of levels are for the C_2 ions, with the leftmost column representing energy values refined by this study. The most complete previous observation of these energy levels are given in the two center columns and are due to the observations of Gruber, et. al.⁶³ The right column of levels is for ions occupying the C_{3i} sites.⁶⁴ The following Zeeman spectroscopy study is concerned with the paramagnetic properties of the Z_1 and Y_1 levels of ions in C_2 sites as the 6512 cm^{-1} transition between these levels is of interest for OCT devices; corresponding levels for ions in C_{3i} sites have been studied by G. Reinemer.⁶⁴

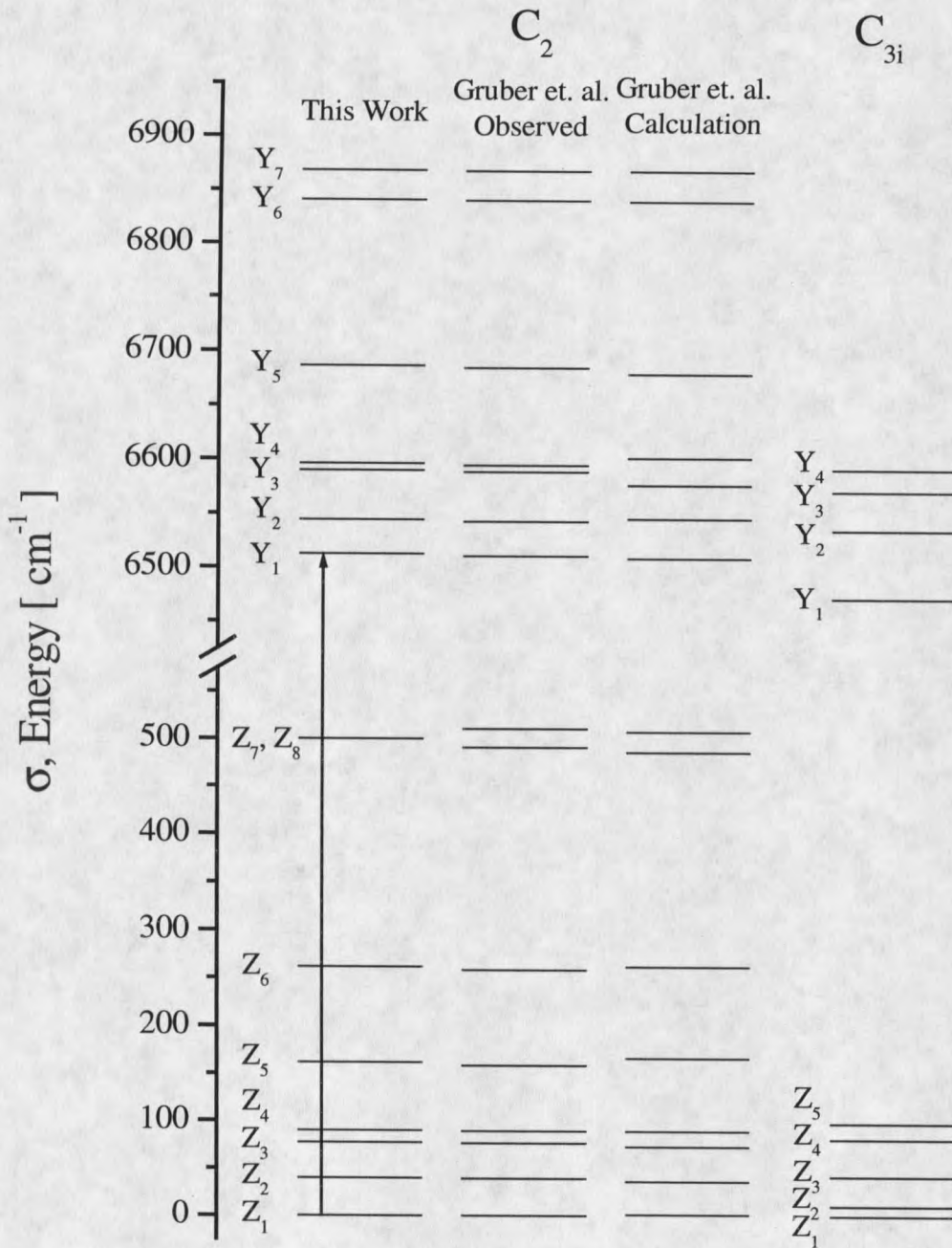


Figure 3.6. Crystal field levels of ${}^4\text{I}_{15/2}$ and ${}^4\text{I}_{13/2}$ multiplets of $\text{Er}^{3+}:\text{Y}_2\text{O}_3$. Deduced from absorption and site selective fluorescence excitation. Leftmost column shows energy levels refined by this work for ions in C_2 sites and the arrow denotes the transition of interest for OCT devices; center two columns are values from Reference 63. Rightmost column shows energy levels of ions in C_{3i} sites studied by G. Reinemer.⁶⁴

Table 3.1. Crystal field levels of 0.005% Er ³⁺ :Y ₂ O ₃				
^S L _J Multiplet	Er ³⁺ in C ₂			Er ³⁺ in C _{3i}
Empirical Designation	This Work	Reference 63 Observed	Reference 63 Calculation	G. Reinemer Reference 64
⁴ I _{15/2} :	Energy [cm ⁻¹]			
Z ₁	0	0	1	0
Z ₂	39.5	39	36	9.9
Z ₃	77.4	76	82	41.0
Z ₄	90.0	89	97	80.6
Z ₅	161.8	158	145	97.3
Z ₆	261.8	258	267	
Z ₇	500	490	486	
Z ₈	(see text)	510	502	
⁴ I _{13/2} :	Energy [cm ⁻¹]			
Y ₁	6512.1	6510	6512	6470.2
Y ₂	6544.5	6542	6545	6534.1
Y ₃	6589.8	6588	6580	6570.2
Y ₄	6596.1	6594	6606	6590.6
Y ₅	6686.4	6684	6676	
Y ₆	6841.0	6840	6840	
Y ₇	6868.0	6867	6842	

Excited State Lifetime

Methods and Apparatus

The crystal used above was placed in the cryostat at 1.5 K to avoid significant population of levels other than the Z₁ ground level. Pumping the ⁴I_{15/2}:Z₁ to ⁴I_{13/2}:Y₂ transition allowed simple spectral discrimination of the fluorescence from the laser excitation. Fluorescence from ⁴I_{13/2}:Y₁ to ⁴I_{15/2} levels occurred after rapid nonradiative

decay from Y_2 to Y_1 . The fluorescence lifetime apparatus is shown in Figure 3.7 and much of it was the same as that shown in Figure 3.4. Model and manufacturer are the same unless specifically stated otherwise. A Crystal Technology Model 3165-1 Acousto-Optic Modulator (AOM) produced 2.5 ms duration pulses, required by the low transition oscillator strength, of 4 mW peak powers from the laser (ECDL) beam at a 10 Hz repetition rate. The 165 MHz drive signal to the modulator was generated by a PTS 500 rf synthesizer (RF). Low voltage pulses from the Hewlett Packard Model 8013B Pulse Generator (HP-PG) controlled the Watkins-Johnson S1 rf switch (SW) gating 2.5-ms rf pulses to the ENI Model 411LA 40 dB rf power amplifier (AMP) which boosted the rf pulses to 5 watts. Fluorescence was collected at 90° to the laser path and focused on the monochromator (SPEX) entrance slit. The monochromator was tuned to the Z_1 to Y_1 transition, and light from the monochromator exit slit was imaged onto the photomultiplier tube (PMT). The 3 ns rise time of the photomultiplier tube provided sufficient response to collect undistorted decays. As a diagnostic, the New Focus 2033 Ge photodiode (GePD) monitored the transmitted laser signal and was used to identify the Z_1 to Y_2 absorption lines by operating the modulator continuous-wave at reduced power and scanning the laser; the photodiode also provided real-time capture of the partially absorbed excitation pulses with the modulator in pulsed mode and the laser tuned to the absorption line center. The photomultiplier tube and photodiode photocurrents were fed to the oscilloscope (SCOPE), which was triggered by the pulse generator. The oscilloscope was interfaced with an 80486-based micro-computer, not

shown, using GPIB IEEE-488 that allowed capture of fluorescence decays, excitation pulses, absorption lines, and background levels.

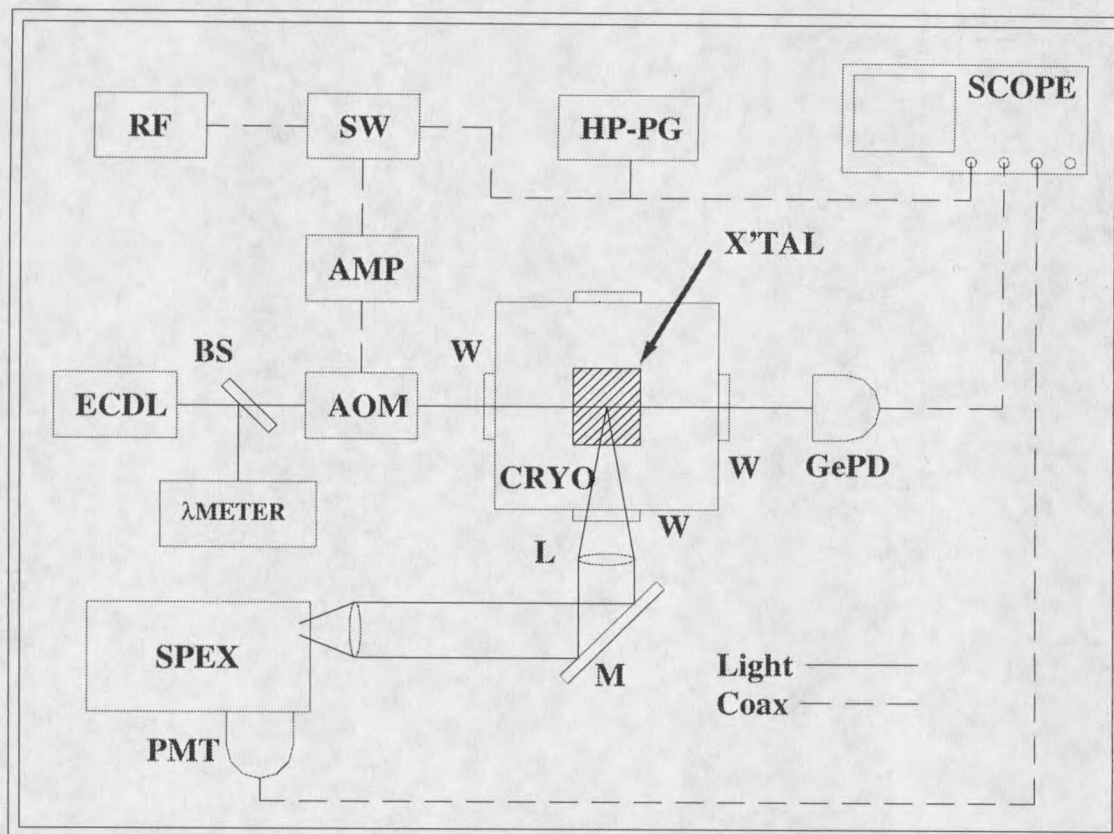


Figure 3.7. Apparatus for measurement of ${}^4I_{13/2}$ fluorescence lifetime T_1 .

Results and Discussion

The normalized single shot fluorescence decay for C_2 sites is shown in the upper graph of Figure 3.8 and is obscured by the photomultiplier noise floor after about 60 ms; the solid line is a non-linear least squares exponential decay fit to the data. A fluorescence lifetime of $T_1 = (8.510 \pm 0.020)$ ms was obtained from the fit, establishing the upper bound for the coherence lifetime of Er^{3+} in C_2 sites at $T_2 \leq 2T_1 = 17.02$ ms,

and is in good agreement with the previously measured value⁷⁴ of (8.000 ± 0.500) ms for 0.2% $\text{Er}^{3+}:\text{Y}_2\text{O}_3$ at 77 K and previously calculated value⁷⁴ of (7.750 ± 2.150) ms. The C_{3i} site fluorescence decay is shown in Figure 3.9 and it gave a $T_1 = (14.620 \pm 0.030)$ ms lifetime. There were no previous measured or calculated values for comparison. The lower graph in each figure shows the normalized transmitted portion of the excitation pulse and the energy level diagram depicting the excitation and fluorescence scheme is shown below the fluorescence decay.

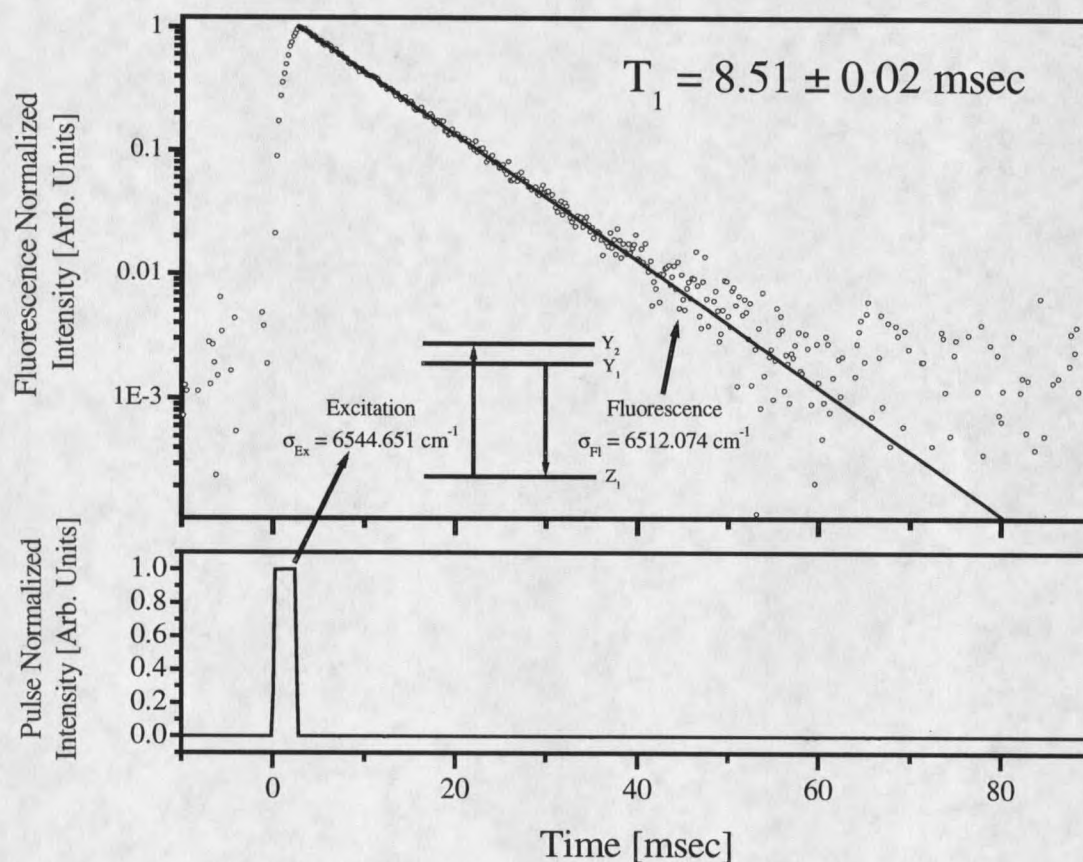


Figure 3.8. Fluorescence lifetime of Er^{3+} in C_2 sites of Y_2O_3 . Upper graph shows 8.51 ms fluorescence decay and energy levels used; lower graph shows the 2.5 ms laser pulse that excited fluorescence.

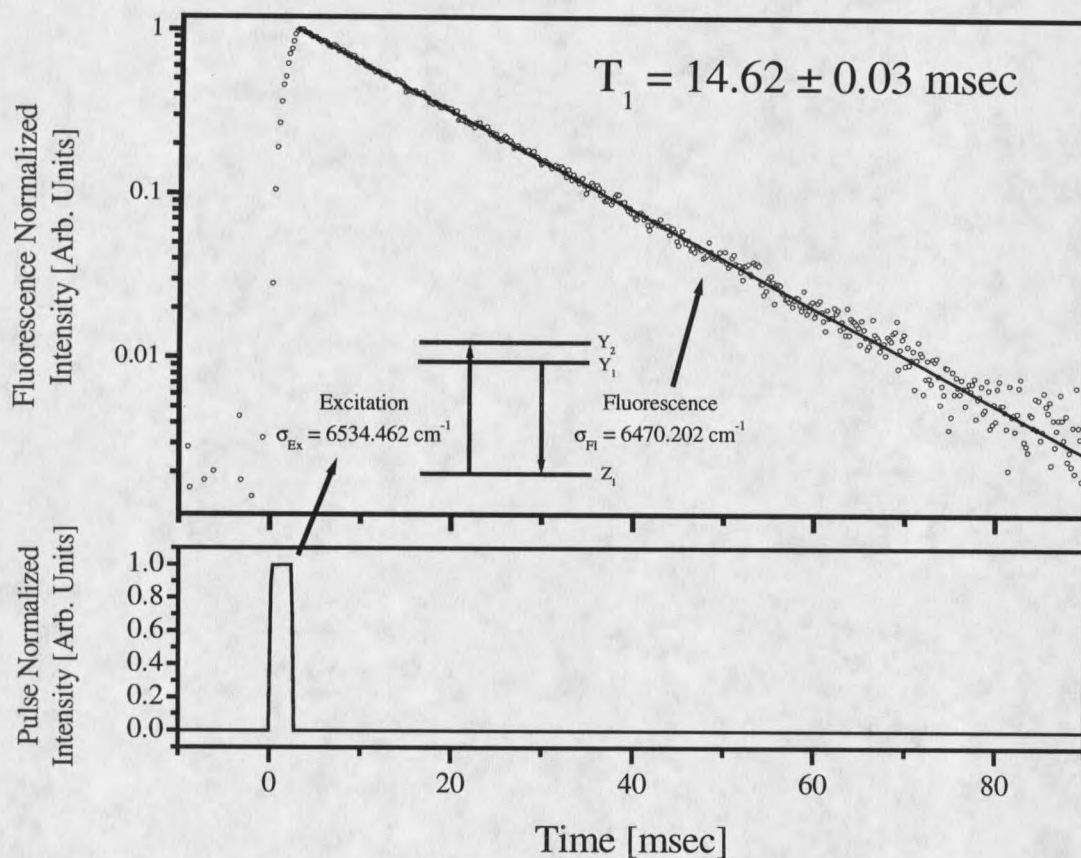


Figure 3.9. Fluorescence lifetime of Er^{3+} in C_{3i} sites of Y_2O_3 . Upper graph shows 14.62 ms fluorescence decay and energy levels used; lower graph shows the 2.5 ms laser pulse that excited fluorescence.

Paramagnetic g-tensors

The Hamiltonian for the Zeeman interaction of a weak applied magnetic field \vec{B} takes the simple form, $\hat{H}_Z = -\vec{\mu}_J \cdot \vec{B}$. Here $\vec{\mu}_J = \mu_B g_J \vec{J}$ is the total magnetic moment operator, μ_B is the Bohr magneton, g_J is the Landé g-factor, and \vec{J} is the total angular momentum. For the free ion the angular momenta J and M_J are good quantum

numbers, and the J -multiplet is split into $2J + 1$ equally spaced Zeeman sub-levels with field dependent energy shifts $\Delta\sigma = \mu_B M_J g_J B$.^{75,76}

This simple picture changes dramatically when the ion is in a crystal. As discussed in Chapter 2 and previously in this chapter, a crystal field partially lifts the $(2J + 1)$ fold degeneracy of the J -multiplet and imposes reduced symmetry so that J and M_J are no longer good quantum numbers.^{16,75,76} The resulting Kramers doublets are each split differently by an external magnetic field. The effective spin Hamiltonian for the weak magnetic field Zeeman effect in a crystal field, ignoring hyperfine structure, becomes:

$$\hat{H}_Z = \mu_B (\vec{S} \cdot \tilde{g} \cdot \vec{B}), \quad (3.1)$$

where \vec{S} is an effective spin ($S = 1/2$), determined by the crystal field level degeneracy in zero field and \tilde{g} is a symmetric rank 2 tensor in Cartesian coordinates determined by the crystal site point symmetry.^{75,77} For a Kramers doublet, $S = 1/2$. A symmetric rank 2 tensor has six independent components, which may be chosen as the three principal axes of an ellipsoid labeled x , y , z and the three angles specifying the ellipsoid orientation with respect to the crystallographic site.^{75,77} For sites of C_2 symmetry, as in Y_2O_3 , one principal ellipsoid axis, by convention the z -axis, must be along the C_2 symmetry axis, and four parameters are left independent: the g -values g_x , g_y , g_z along the principal axes and a single angle α orienting the tensor x - y principal axes with respect to the crystallographic axes.⁷⁵ Each crystal field level has distinct values of g_x , g_y , g_z , and α . In Y_2O_3 the \tilde{g} -tensor z -axis is along $[100]$ for the 5 and 6 sites, $[010]$ for the 7 and

8 sites, and [001] for the 9 and 10 sites according to the convention of Figure 3.1. For each site, the Zeeman Hamiltonian in Equation 3.1 can be written in terms of the principal g-values as:

$$\hat{H}_Z = \mu_B (g_x S_x B_x + g_y S_y B_y + g_z S_z B_z) \quad (3.2)$$

where S_x , S_y , S_z are effective spin operator components and B_x , B_y , B_z are the applied magnetic field components.⁷⁵ Each crystal field level splits into two Zeeman sub-levels with magnetic field and orientation dependent energy shifts given by:

$$\Delta\sigma = \pm \frac{\mu_B}{2} g_i |B| \quad (3.3)$$

where $\Delta\sigma$, the energy level shift, is typically given in wavenumbers, $|B|$ is the magnetic field strength and g_i , $i=5,\dots,10$ is the orientation dependent g-value for each site as given below.

To aid in the following discussion a graphical interpretation of the g-tensors is presented in Figure 3.10 and reference to Figure 3.3 is useful. Six rectangular solids, or "bricks," are numbered to associate each with one of the six C_2 sites; the dimensions of the bricks are scaled to match the ground state principal g-values, as measured by EPR⁵⁸ ($g_x = 1.645$, $g_y = 4.892$, $g_z = 12.314$). The bricks are shown realistically oriented with respect to the $\langle 100 \rangle$ crystal axes except that the 2° tipping angle α measured⁵⁸ for this state has been exaggerated to 20° (in reality $+2^\circ$ from EPR⁵⁸) for illustration purposes. Specifically, the C_2 axis of site 10 is parallel with [100]; the site 10 ellipsoid is tipped $+2^\circ$ (for illustration $+20^\circ$) from [001] toward [010].

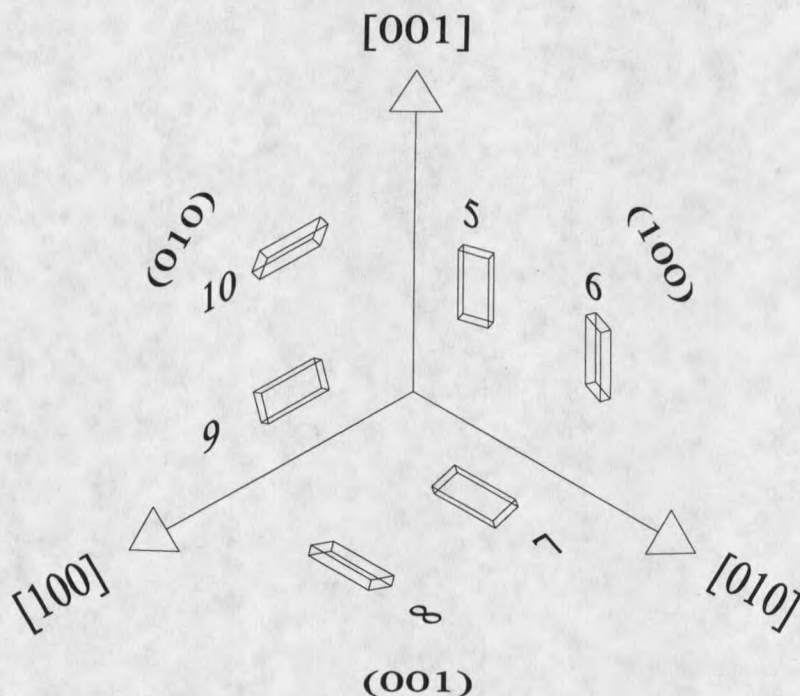


Figure 3.10. Graphical representation of g -tensor orientation with respect to crystal axes for the six C_2 sites in Y_2O_3 for $Er^{3+} {}^4I_{15/2}; Z_1$. Tipping angle α exaggerated for illustration. Viewed along $[111]$, orientational equivalence of sets comprised of sites labeled 5, 7, 9 and 6, 8, 10 for $B \parallel [111]$ is evident.

It is useful to express the field dependent eigenvalues as ellipsoidal equations.⁷⁷ The projections of an applied magnetic field on the primary axes, dimensions of the bricks, of each orientationally inequivalent site are orientation dependent; the ellipsoidal equations are written directly as the summed squares of these projections. With the magnetic field applied in the (001) plane, the orientation dependent g -values for each site (g_5, \dots, g_{10}) are expressed as:⁵⁸

$$g_{5/6}^2 = g_x^2 \cos^2(\Phi \mp \alpha) + g_y^2 \sin^2(\Phi \pm \alpha) \quad (3.4a)$$

$$g_7^2 = g_8^2 = g_z^2 \sin^2 \Phi + (g_y^2 \cos^2 \alpha + g_x^2 \sin^2 \alpha) \cos^2 \Phi \quad (3.4b)$$

$$g_9^2 = g_{10}^2 = g_z^2 \cos^2 \Phi + (g_x^2 \cos^2 \alpha + g_y^2 \sin^2 \alpha) \sin^2 \Phi. \quad (3.4c)$$

Equations 3.4 apply to both the ground and excited states, with different principal g -values g_x, g_y, g_z and tipping angles α . Here Φ is the angle between the applied magnetic field and the $[100]$ axis in the (001) plane. For the bricks labeled 9 and 10 the longest dimension g_z is along the field when $\Phi = 0^\circ$ and this orientation yields pure measurements of g_z ; the projection of g_z for the 9 and 10 bricks onto the field vanishes as Φ increases to 90° but the projection of g_z along the field for bricks labeled 7 and 8 maximizes again yielding a pure measurement of g_z , but using ions labeled 7 and 8. It is instructive to note that the ions labeled 7 and 8, with their C_2 axes along $[010]$, and the ions labeled 9 and 10, with their C_2 axes along $[100]$, are orientationally equivalent with respect to the (001) plane. Also, with $\Phi = 0^\circ$ and 90° the ions labeled 5 and 6 become orientationally equivalent.

Similarly, when the applied magnetic field is in the (110) plane, the g -values for the various sites can be expressed as:⁵⁸

$$g_{5/6}^2 = g_z^2 \cos^2 \Theta + \left\{ g_x^2 \cos^2 \left(\frac{\pi}{4} \pm \alpha \right) + g_y^2 \sin^2 \left(\frac{\pi}{4} \pm \alpha \right) \right\} \sin^2 \Theta \quad (3.5a)$$

$$g_{7/8}^2 = \left(\cos \Theta \cos \alpha \mp \frac{1}{\sqrt{2}} \sin \Theta \sin \alpha \right)^2 g_x^2 + \left(\pm \cos \Theta \sin \alpha + \frac{1}{\sqrt{2}} \sin \Theta \cos \alpha \right)^2 g_y^2 + \frac{1}{2} g_z^2 \sin^2 \Theta \quad (3.5b)$$

$$\begin{aligned}
g_{9/10}^2 = & \left(\cos \Theta \cos \alpha \pm \frac{1}{\sqrt{2}} \sin \Theta \sin \alpha \right)^2 g_y^2 \\
& + \left(\mp \cos \Theta \sin \alpha + \frac{1}{\sqrt{2}} \sin \Theta \cos \alpha \right)^2 g_x^2 + \frac{1}{2} g_z^2 \sin^2 \Theta
\end{aligned} \tag{3.5c}$$

Again, these equations apply to all crystal field levels. In this case Θ is the angle between \vec{B} and the $[001]$ axis in the (110) plane. All six sets of ions are orientationally inequivalent with respect to this plane. Special orientations somewhat reduce the six-fold inequivalence. The pairs 5 and 6, 7 and 8, and 9 and 10 collapse into three inequivalent sets at $\Theta = 0^\circ$ and g_z can be directly measured of using the sets labeled 5 and 6. The sites labeled 7 and 8 and 9 and 10 are equivalent when $\Theta = \pm 90^\circ$. Finally, and most interestingly, at $\Theta = \pm 54.7^\circ$, where \vec{B} is along $[\bar{1}11]$ or $[1\bar{1}1]$, the inequivalence is only two-fold with the ions 5,7 and 9 forming a single equivalent set and the ions 6,8 and 10 forming a distinct set as can be clearly seen in Figure 3.10.

A transition-labeling scheme aided collection and analysis of the 24 possible transitions, four from each of the six sites, between the two Zeeman components of the ground and excited states. The "a" transition, from the ground state lower component ($Z_{1\downarrow}$) to the excited state higher component ($Y_{1\uparrow}$), had the highest energy of the four. The lowest energy transition, $Z_{1\uparrow}$ to $Y_{1\downarrow}$, was the "d" line. The "b" transition ($Z_{1\downarrow}$ to $Y_{1\downarrow}$) was typically higher energy than the "c" transition ($Z_{1\uparrow}$ to $Y_{1\uparrow}$) as the ground state g-value was typically greater than the excited state g-value; but the reverse was true for orientations where the excited state ellipsoid protruded from the ground state ellipsoid.

A subscript, 5-10, was added to each letter designation making the label site-specific and transition labels are grouped when sites are magnetically equivalent.

The orientation and field dependent transition energies were calculated to first order by combining Equations 3.4 and 3.5 with Equation 3.3. The a and d transition energies are:

$$\sigma_i^{(a,d)}(\Phi \text{ or } \Theta) = \sigma_0 \pm ({}^s\Delta\sigma + {}^e\Delta\sigma) = \sigma_0 \pm \frac{\mu_B}{2} ({}^s g_i + {}^e g_i) B \quad (3.6a)$$

and + corresponds to a and – to d. The b and c transition energies are:

$$\sigma_i^{(b,c)}(\Phi \text{ or } \Theta) = \sigma_0 \pm ({}^s\Delta\sigma - {}^e\Delta\sigma) = \sigma_0 \pm \frac{\mu_B}{2} ({}^s g_i - {}^e g_i) B \quad (3.6b)$$

and + corresponds to b and – to c. The ground (excited) state g-values, ${}^s g_i$ (${}^e g_i$), for sites $i = 5, \dots, 10$, are substituted from Equations 3.4 (3.5), σ_0 is the zero-field Z_1 to Y_1 transition energy. Graphs of $\sigma_i^{(a,d)}(\Phi \text{ or } \Theta)$ and $\sigma_i^{(b,c)}(\Phi \text{ or } \Theta)$, using estimated ${}^s g$ and ${}^e g$ values, provided excellent guides for assigning and tracking transitions during data collection; initial values for $({}^s g_x, {}^s g_y, {}^s g_z; {}^s \alpha)$ and $({}^e g_x, {}^e g_y, {}^e g_z; {}^e \alpha)$ were adjusted and plots updated in real-time as the data were collected. Initial ground state values relied on published EPR values^{58,59} and excited state principal g-values were previously unmeasured.

Determination of the ground and excited state \tilde{g} -tensor principal parameters, $({}^s g_x, {}^s g_y, {}^s g_z; {}^s \alpha)$ and $({}^e g_x, {}^e g_y, {}^e g_z; {}^e \alpha)$, respectively was accomplished by analyzing orientation dependent Zeeman absorption spectra. Ground (excited) state g-values were calculated by subtracting energies of transitions connecting different ground (excited)

state Zeeman components with the same excited (ground) state component. There were two ways to calculate each g-value:

$${}^s g_i(\Phi \text{ or } \Theta) = \frac{(\sigma_i^{(a)} - \sigma_i^{(c)})}{\mu_B B} = \frac{(\sigma_i^{(b)} - \sigma_i^{(d)})}{\mu_B B} \quad (3.7a)$$

and

$${}^e g_i(\Phi \text{ or } \Theta) = \frac{(\sigma_i^{(a)} - \sigma_i^{(b)})}{\mu_B B} = \frac{(\sigma_i^{(c)} - \sigma_i^{(d)})}{\mu_B B} \quad (3.7b)$$

Methods and Apparatus

Two larger crystals from the same commercial growth as the crystal used in determining crystal field levels and upper state lifetime were used for measurement of Z_1 and Y_1 \tilde{g} -tensors and were oriented by Laue X-ray diffraction. The "001-crystal" and "110-crystal" were oriented for applying the magnetic field in the (001) and (110) planes, respectively, and to provide optical access, propagation and maximum absorption along [001] and [110], respectively. The 001-crystal was cut and ground into a rectangular solid with dimensions of 8.84 mm along [001], 5.08 mm along [110] and 3.76 mm along $[1\bar{1}0]$. The 110-crystal was cut and ground into a rectangular solid with dimensions of 8.25 mm along [110], 4.65 mm along $[1\bar{1}0]$ and 3.95 mm along [001]. Faces normal to the optical propagation direction were polished to optical inspection quality with 1.0 μm alumina paste to reduce scatter. The remaining four crystal faces were simply ground flat with 600 grit silicon carbide paper.

The Zeeman spectroscopy apparatus is shown in Figure 3.11 and included many of the components used in absorption and fluorescence above. The crystals were mounted one at a time in an Oxford Instruments SpectroMag cryostat (CRYO). The SpectroMag provided stable temperatures from 1.5 K with superfluid helium immersion to 300 K using the built-in resistive electrical heater, helium gas flow controls, and the attached vacuum pump. The SpectroMag's superconducting solenoid had its \vec{B} field oriented in the horizontal plane and provided fields up to 8 Tesla. Optical access to the crystal was through an opposing pair of windows (W) centered in the horizontal plane along an axis orthogonal to the magnet axis.

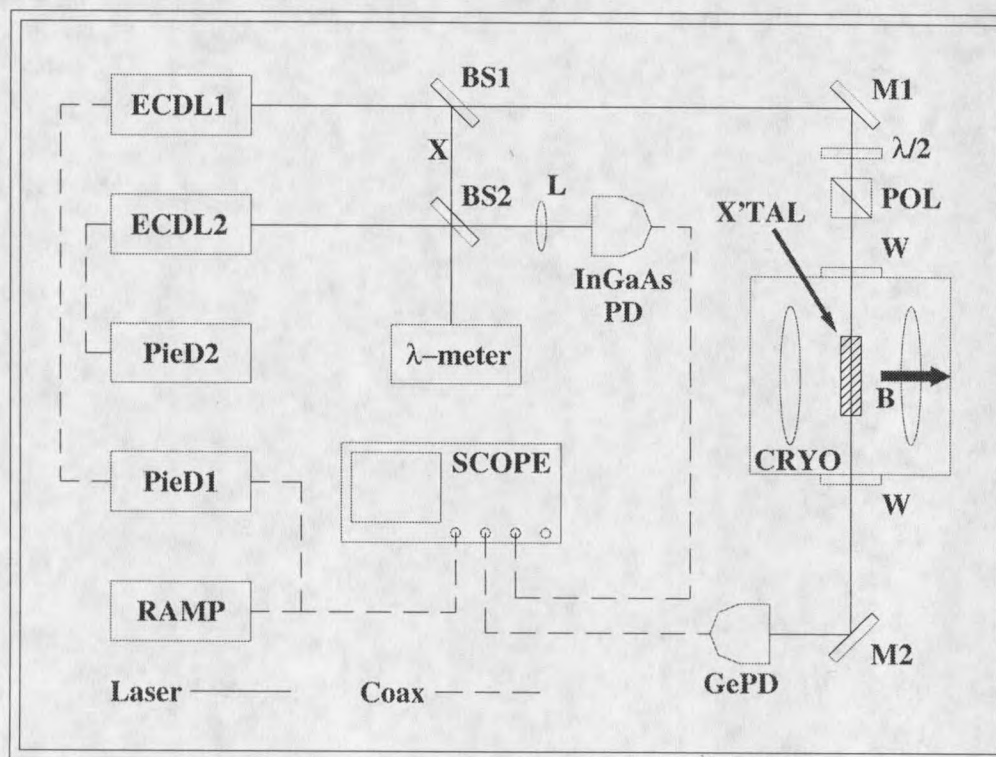


Figure 3.11. Apparatus for $\text{Er}^{3+} \ ^4\text{I}_{15/2} - \ ^4\text{I}_{13/2}$ Zeeman spectroscopy including one laser for measurement of sample absorption and a second for calibration of optical frequency.

Thermal population of the ground state upper Zeeman component was required to observe all four Zeeman transitions for a specific site, and to achieve this the crystals were typically held between 6 and 7 K at a magnetic field of 1 T. Varying the temperature and magnetic field strength allowed determination of the originating and terminating levels of the Zeeman transitions. Lowering the temperature or increasing magnetic field diminished transitions originating in the upper Zeeman component of the ground state and strengthened transitions originating in the lower Zeeman component.

A custom-built sample rod allowed rotation of the crystal about two orthogonal axes. The entire rod could be rotated about the concentric vertical cryostat axis and positioned with care to $\pm 1^\circ$; this allowed rotation of the sample in the horizontal plane and alignment of the second rotation axis orthogonal to the magnetic field. This second rotation axis was along the axis of a hollow cylindrical crystal holder; rotating a shaft, internal and concentric to the main rod, rotated the crystal holder and crystal in the magnetic field. Bevel gear teeth on the internal shaft end and crystal holder outer perimeter provided a 2.5:1 gear ratio. Taking care to avoid gear backlash, the internal shaft could be reproducibly positioned to the equivalent of $\pm 0.2^\circ$ of crystal rotation; a vernier scale was attached to the internal shaft and a scale was attached to the main rod, inscribed with divisions corresponding to 0.1° and 1° increments of crystal rotation, respectively.⁷⁷ The brass geared shaft and crystal holder were provided by Dr. M. J. M. Leask of the Clarendon Laboratory at the University of Oxford, United Kingdom. The remaining sample rod parts were brass and stainless steel joined by silver solder and were designed specifically for this experiment.

The Zeeman spectra were recorded with a Littman-Metcalf external cavity diode laser⁶⁶⁻⁷¹ (ECDL1) that provided up to 5 mW single mode output between 1500 and 1575 nm with a jitter limited linewidth of < 200 kHz. This laser was tuned by moving the roof prism retro-reflector by either a fine pitch screw, providing better than 5 GHz resolution, or by a piezoelectric stack, giving mode-hop free scans of up to 46 GHz and scan repetition rates up to a few hundred Hertz.

A Stanford Research Systems DS345 (RAMP) synthesizer generated a ± 5 volt, 10 Hz triangular wave that the Thor Labs Piezo Driver Model MDT 691 (PieD1) converted to a 0-150 volt triangular wave, and applied to the laser to scan it full-range. Beam-splitter (BS1) split a portion of the scan laser output power to mirror M1. A half-wave plate ($\lambda/2$) rotated the polarization of the linearly polarized beam and the Glan-Thomson polarization analyzer (POL) was used to verify polarization of transitions along or orthogonal to the magnetic field. The hollow cylindrical crystal holder masked the crystal, and the collimated laser beam passed through the crystal, and cryostat, and was detected by the NewFocus 2033 germanium photodiode (GePD). The laser scan rate and the 200 kHz photodiode bandwidth allowed collection of undistorted transmission spectra. The Tektronix TDS520D oscilloscope (SCOPE) displayed spectra in real-time with triggering from the synthesizer; the GPIB IEEE-488 interface with an 80486-based personal computer (not shown) allowed data recording. The large-area photodiode and real-time spectral display allowed observation and identification of transitions while rotating the crystal in the applied magnetic field.

A special procedure was developed for accurate calibration of the scan laser wavelength. The deflected portion of the scan laser at the first beam splitter (BS1) was combined at a second beam splitter (BS2) with the output of a second identical laser, the marker laser, and split into two beams; one beam was focused by lens L onto a NewFocus 1811 InGaAs photodiode (InGaAs PD) and the other was fiber coupled into a Burleigh WA-1500 wavemeter (λ -meter). The oscilloscope displayed the two-laser beat when the marker laser was tuned to the scan laser within the 125 MHz bandwidth of the InGaAs photodiode. Adjusting the voltage of the second Thor Labs Piezo Driver Model MDT 691 (PieD2) tuned the marker laser and tuned the beat in real-time allowing measurement of frequencies at any position in the scan. Transition energies were measured by blocking the scan laser at position X (Figure 3.11) and recording the absolute frequency of the marker laser, measured by the wavemeter. Repeatability of transition energy measurements was $\pm 0.001 \text{ cm}^{-1}$ which is nearly the 0.1 ppm accuracy of the wavemeter.

Results

The upper trace of Figure 3.12 is the zero field C_2 site absorption spectrum showing the Z_1 to Y_1 transition at 6512.074 cm^{-1} . The background periodic structure was caused by two etalons, one formed by the cryostat windows with a $\sim 2 \text{ cm}^{-1}$ free spectral range. The parallel entrance and exit surfaces of a beam splitter cube at the output of the scan laser, not shown in Figure 3.12, formed the second étalon with a $\sim 6 \text{ GHz}$ free spectral range. The lower trace is the photodiode noise floor. A thick crystal was required to observe the individual weaker Zeeman transitions with good signal strength at high field

where the degeneracies were lifted; the very strong zero field absorption shown in Figure 3.12 resulted from using the thick crystal but caused no problems when the field was applied.

Typical Zeeman spectra, centered on the zero field transition energy with $B = 1.0$ T in the (001) plane along [100] are given in Figure 3.13, and the top and bottom traces are with polarization perpendicular and parallel to [100], respectively. The b and c transitions for sites 5, 6, 7, and 8 exhibit strongly polarization dependent absorption, but transition energies were never observed to shift with polarization. Two higher energy (a_7a_8 and a_9a_{10}) and two lower energy (d_7d_8 and d_9d_{10}) transitions were outside the 46 GHz scan range and the laser was tuned individually to these outlying transitions to measure their energies.

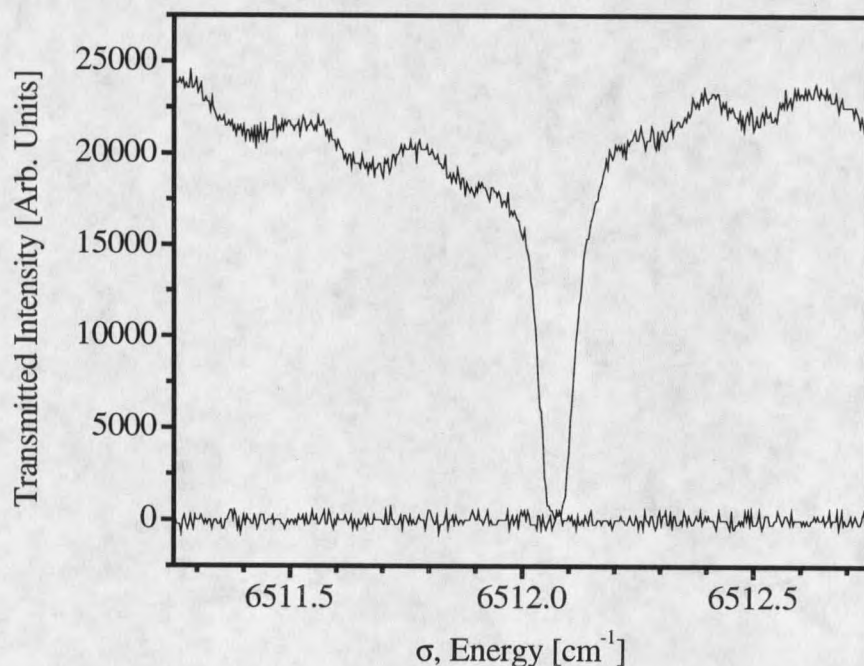


Figure 3.12. Zero field absorption spectrum: C_2 site Z_1 to Y_1 transition at 6512.074 cm^{-1} . Top trace is absorption spectrum and bottom trace is detection noise floor.

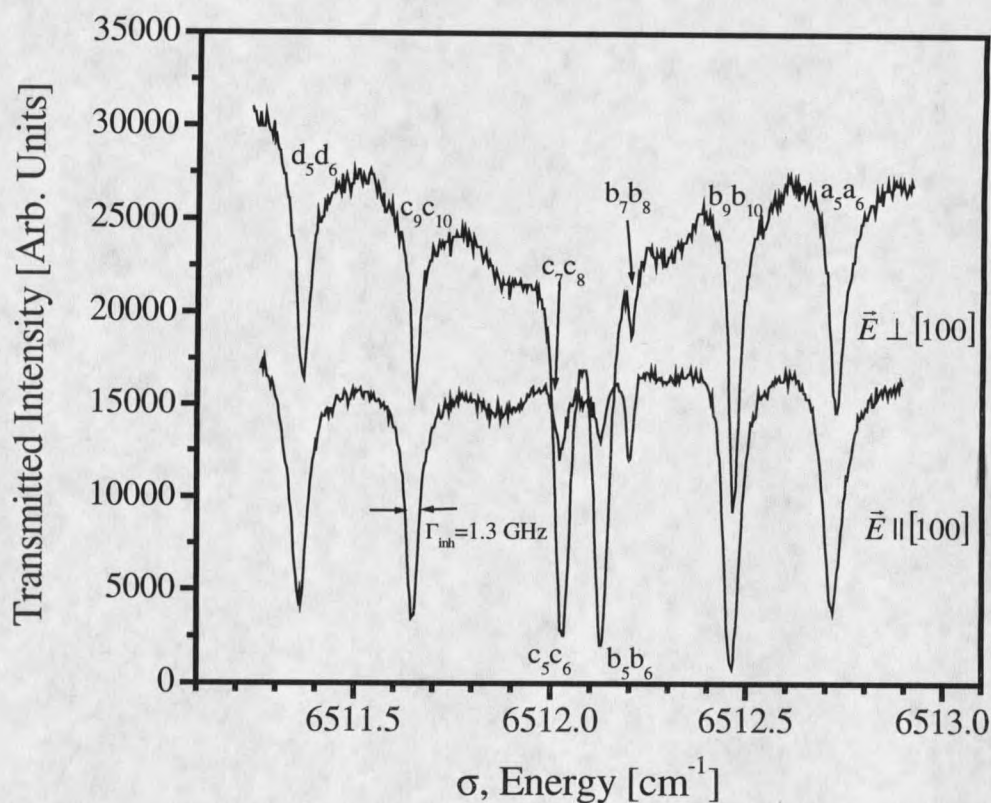


Figure 3.13. Typical Zeeman spectra of $\text{Er}^{3+}:\text{Y}_2\text{O}_3$ with $\vec{B} = 1.0$ T along $[100]$. Upper (lower) trace is with the laser polarized perpendicular (parallel) to the external magnetic field. Transitions are labeled according to site. The “a” and “d” transitions for ions in sites 9 and 10 lie at higher and lower energy, respectively.

To establish validity of the spin Hamiltonian assumed in Equation 3.1, Zeeman spectra were collected at several fields up to 2.0 Tesla with \vec{B} in the (001) plane along $[100]$. The upper, middle and lower subplots in Figure 3.14 present transition energy dependence on magnetic field for ions in sites labeled (5,6), (7,8), and (9,10), respectively; circles are measured transition energies, dotted lines are linear fits to the data, labeled as usual, and solid lines are the zero field transition energy, 6512.074 cm^{-1} .

The assumed Hamiltonian is justified to at least 2.0 Tesla as nearly all transitions, particularly those most field dependent at this orientation, the a_9a_{10} and d_9d_{10} transitions, shift quite linearly with field; the $Z_{1\uparrow}$ level began thermally depopulating beyond 2.0 Tesla making observation of transitions originating in it difficult. Only the b_5b_6 and c_5c_6 transitions display any significant deviation from linearity at these fields. These deviations are not clearly quadratic in nature, and are not accounted for by the scale of the etalon-induced distortions described previously and most evident in Figure 3.12. This is evidence that terms quadratic in field must be added to the Hamiltonian of Equation 3.1 to fully describe the Zeeman splitting behavior at these fields.

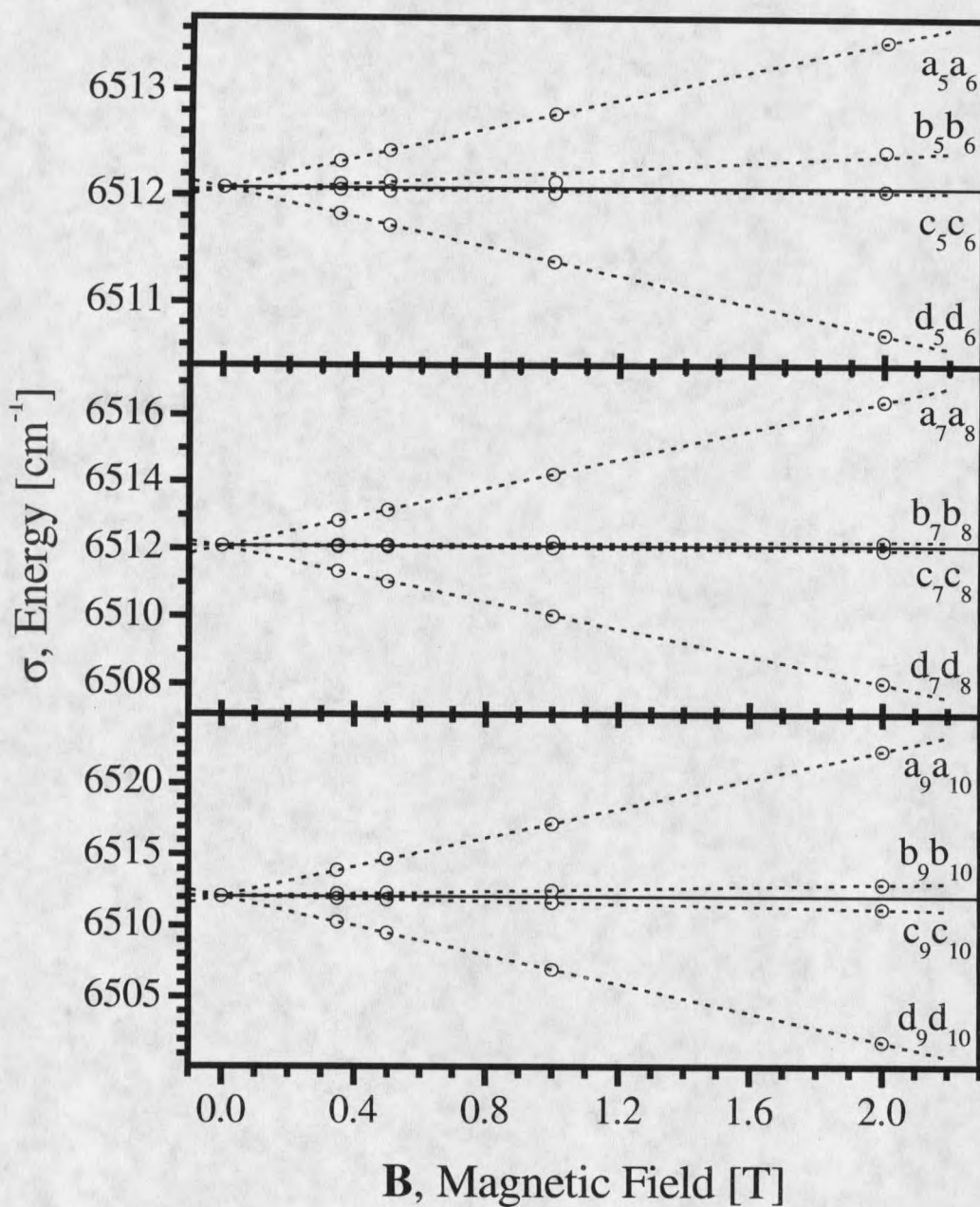


Figure 3.14. Zeeman spectra of $\text{Er}^{3+}:\text{Y}_2\text{O}_3$ vs. magnetic field strength for $\vec{B} \parallel [100]$. Top graph shows absorption lines of ions in sites 5 and 6, middle graph is for ions in sites 7 and 8, and bottom is for ions in sites 9 and 10. Note the energy scale difference in the different graphs.

Complete orientation dependent Zeeman spectra with a 1.0 Tesla external magnetic field applied in the (001) plane are presented in Figure 3.15. Symbols (○) indicate transition energies assigned to observed absorption lines at a particular orientation. Using Equations 3.7 these data were used to calculate orientation dependent g-values, which are presented below. Substituting the best-fit principal values, also presented below, into Equations 3.6 generates the solid curves; transition labels are inset in each solid curve. Figure 3.16 presents transitions b and c (* in Figure 3.15) expanded for clarity; a straight line illustrates zero-field transition energy, $\sigma_0 = 6512.074 \text{ cm}^{-1}$. The b_5 and c_5 (b_6 and c_6) curves cross each other at the zero-field transition energy indicating larger excited state splitting than ground state splitting between $\Phi \sim 5^\circ$ and 65° (115° and 175°) for site 5 (6) ions and excited state ellipsoid protrusion through the ground state ellipsoid. Bars are attached to one data point to illustrate the $\sim 1.3 \text{ GHz}$ inhomogeneous linewidth, but the measurement uncertainty is much smaller, about $\pm 100 \text{ MHz}$ (0.003 cm^{-1}). The site 5, 6 transitions shift to higher energy at $\Phi = 90^\circ$ and the 7, 8 transitions behave similarly at $\Phi = 0^\circ$ and 180° . With the magnetic field in the (110) plane Zeeman spectra were collected more sparsely as the principal \tilde{g} -tensor parameters were well determined by fitting the (001) data. Figure 3.17 presents the (110) spectra and transitions b and c (*) are displayed in Figure 3.18 expanded for clarity; again, a straight line illustrates zero-field transition energy.

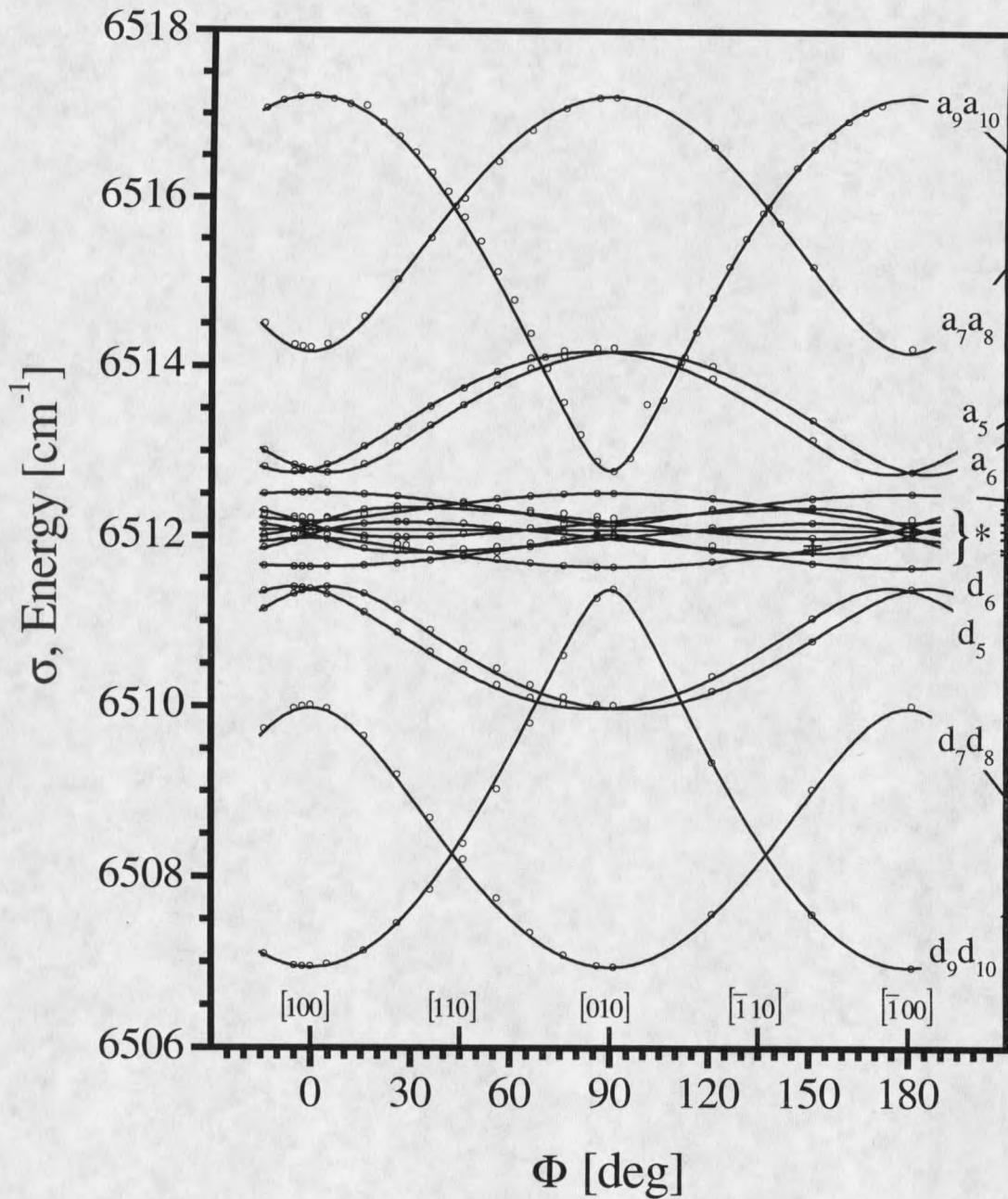


Figure 3.15. Full orientation dependent Zeeman absorption spectra for $\vec{B} = 1.0$ T in (001). Measured transition energies are open circles (\circ) and solid curves are calculated from best fit to g -values. Site-specific transition labels are inset in each curve. Detail (*) of b and c transitions is expanded in Figure 3.16 for clarity.

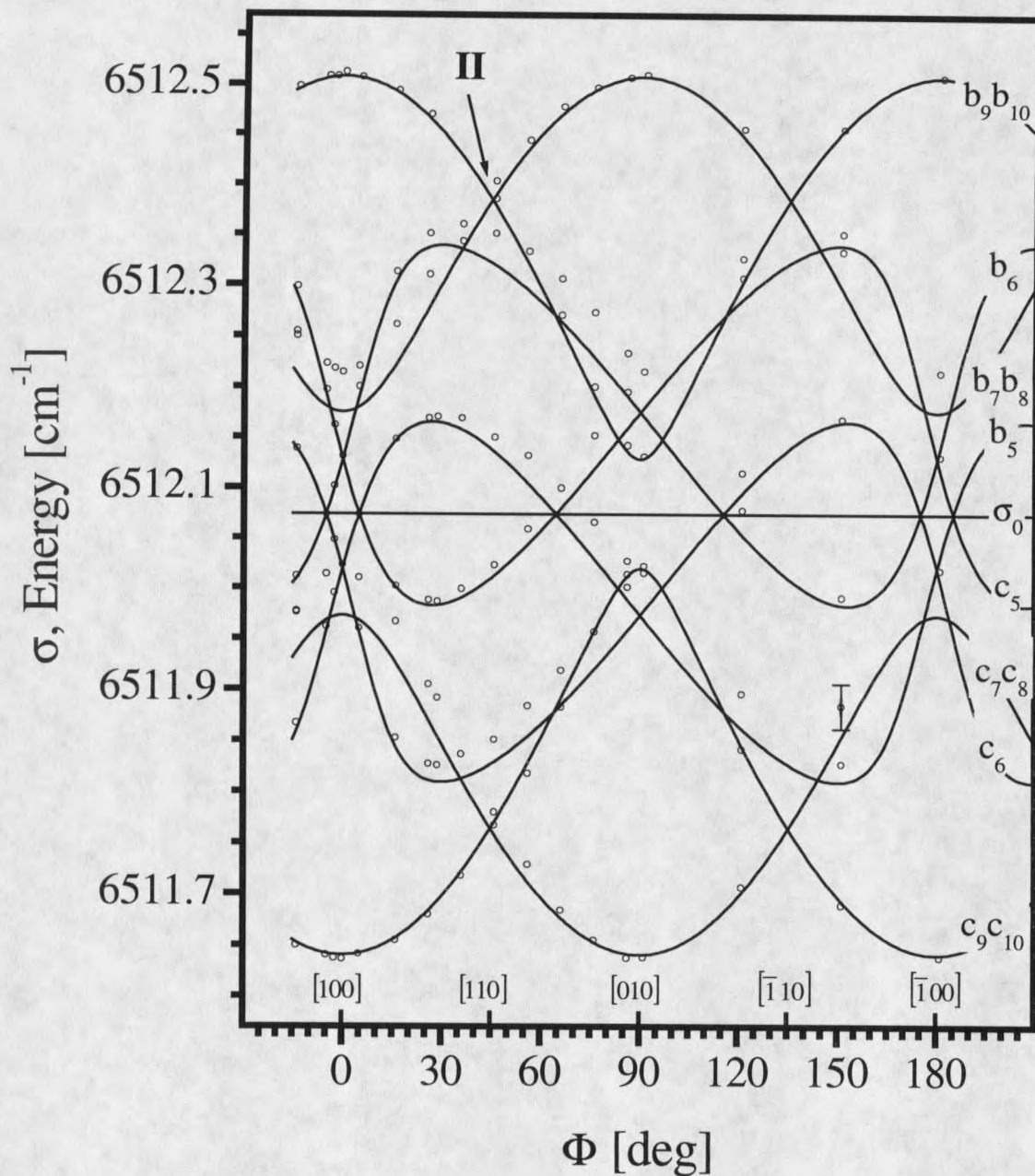


Figure 3.16. Detail (* in Figure 3.15) of orientation dependent Zeeman spectra including b and c transitions with $\vec{B} = 1.0$ T in (001) expanded for clarity. Measured transition energies are open circles (\circ) and solid curves are calculated from g-value best fit. Site-specific transition labels are inset in each curve. A straight line represents the zero field transition energy σ_0 . Bars attached to one data point illustrate the 1.3 GHz inhomogeneous linewidth. Transition and orientation that may optimize coherence lifetime are labeled by **II**.

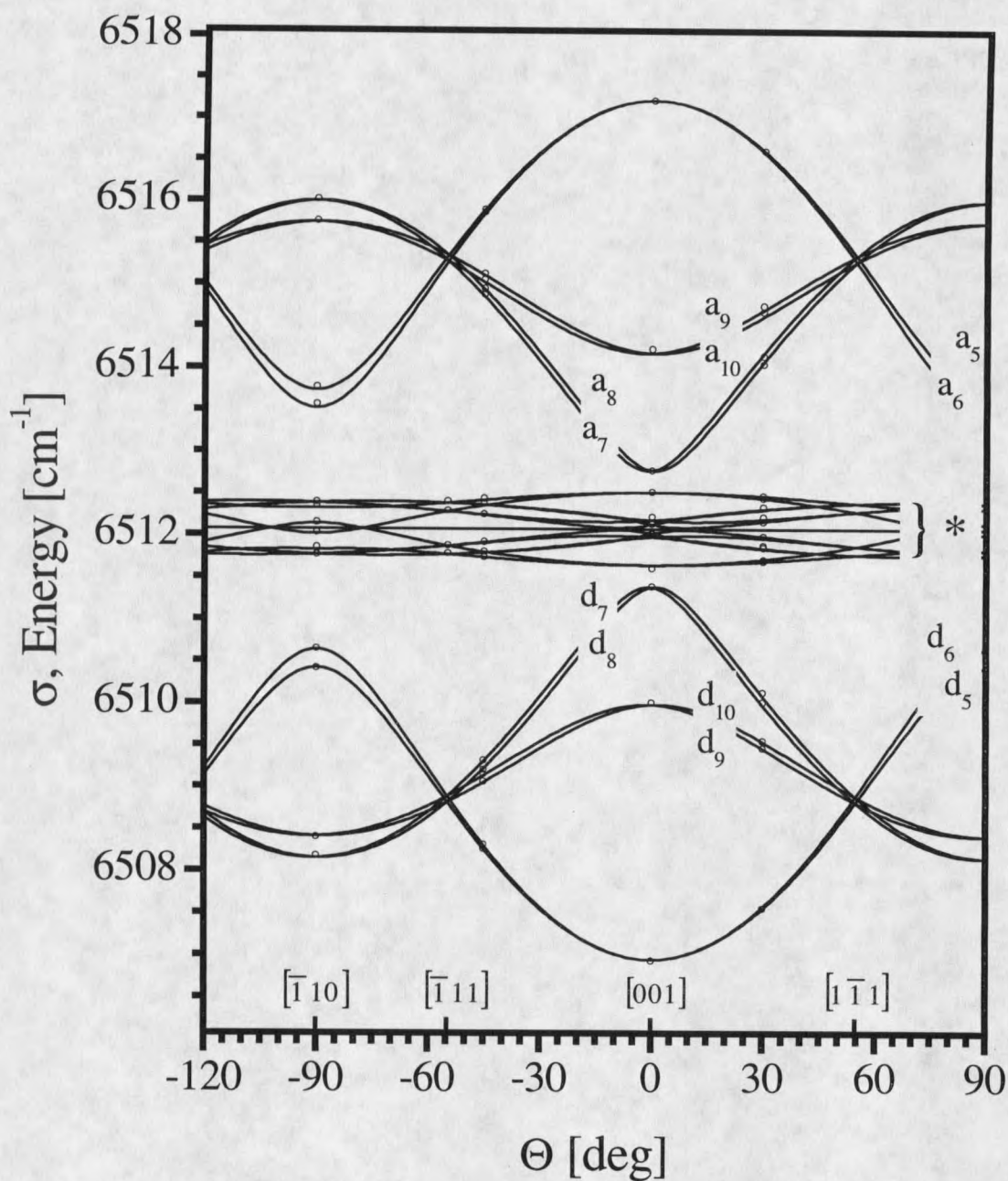


Figure 3.17. Full orientation dependent Zeeman absorption spectra for $\vec{B} = 1.0$ T in (110) . Measured transition energies are open circles (\circ) and solid curves are calculated from g-value best fit. Site-specific transition labels are inset in each curve. Detail (*) of b and c transitions is expanded in Figure 3.18 for clarity.

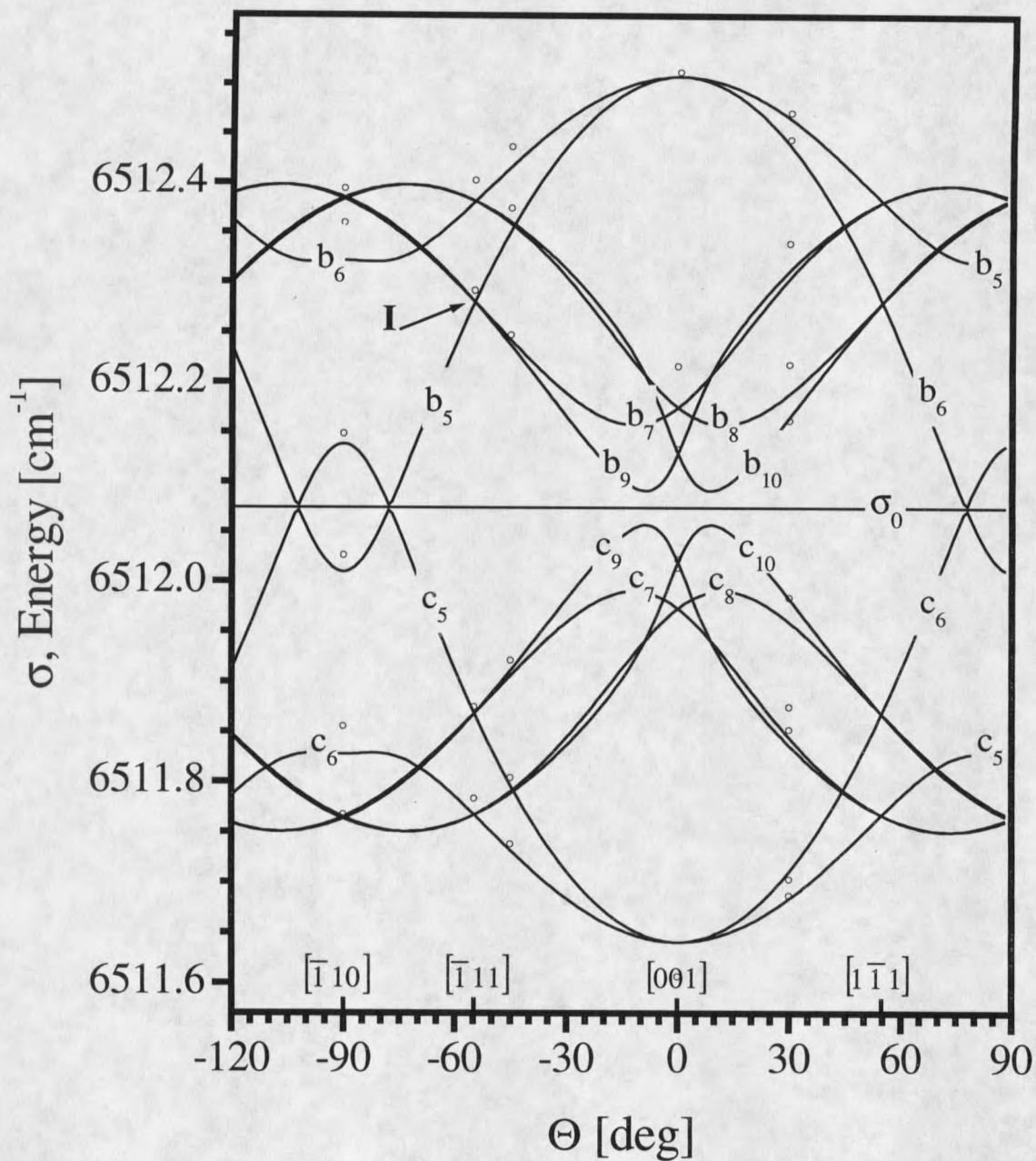


Figure 3.18. Detail (* in Figure 3.17) of orientation dependent Zeeman spectra including b and c transitions with $\vec{B} = 1.0$ T in (110) expanded for clarity. Measured transition energies are open circles (\circ) and solid curves are calculated from g-value best fit. Site-specific transition labels are inset in each curve. A straight line represents the zero field transition energy σ_0 . Transition and orientation that may optimize coherence lifetime are labeled by I.

Figures 3.19 and 3.20 present the (001) plane orientation dependent ground and excited state g-value results, respectively; solid curves are Equations 3.4 using best-fit principal values, and the site-labels, ${}^s g_i$ and ${}^e g_i$, are inset. The g_z principal value can be read directly from the maxima of the 9 and 10 (7 and 8) curves at $\Phi = 0^\circ$ ($\Phi = 90^\circ$), and the different ground and excited state tipping angles, ${}^s \alpha$ and ${}^e \alpha$, allowed by the C_2 point symmetry are evident in curves 5 and 6. Figure 3.21 and 3.22 present graphical representations of the ground and excited state ellipsoids, respectively; again the dimensions of the "bricks" represent the principal g-values and the tipping angles ${}^s \alpha$ and ${}^e \alpha$ are in the opposite sense for the two states and exaggerated (to 20° and -30° , respectively) for illustration purposes. Figures 3.23 and 3.24 present (110) plane ground and excited state g-values, respectively; solid curves are Equations 3.5 with best-fit principal values. The six-fold orientational inequivalence with respect to (110) is more easily observed in the excited state than in the ground state.

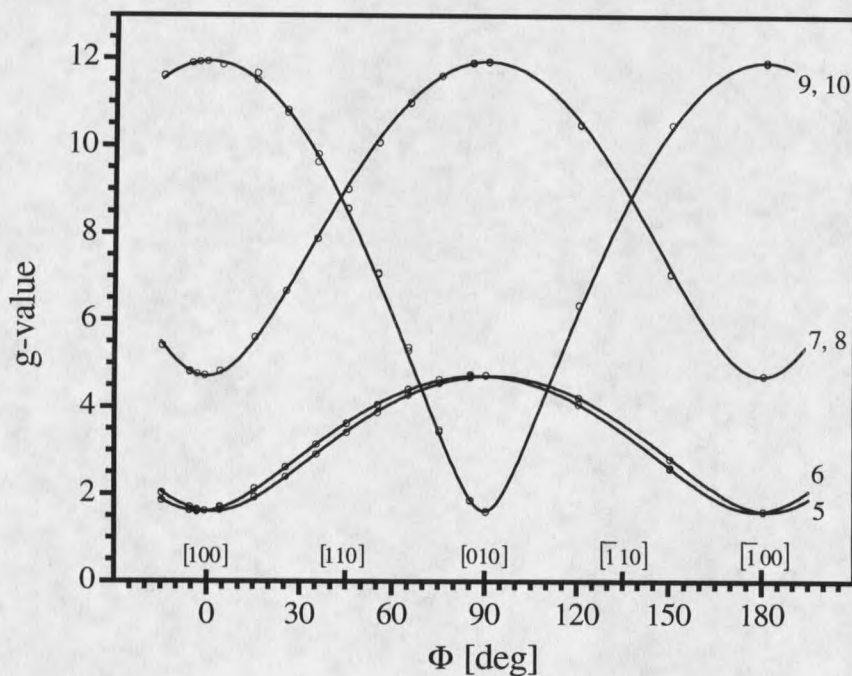


Figure 3.19. g-values for ${}^4I_{15/2}:Z_1$ with field in (001). Symbols (\circ) are data calculated from Zeeman spectra in Figure 3.15; solid curves are best fit. Site labels are inset.

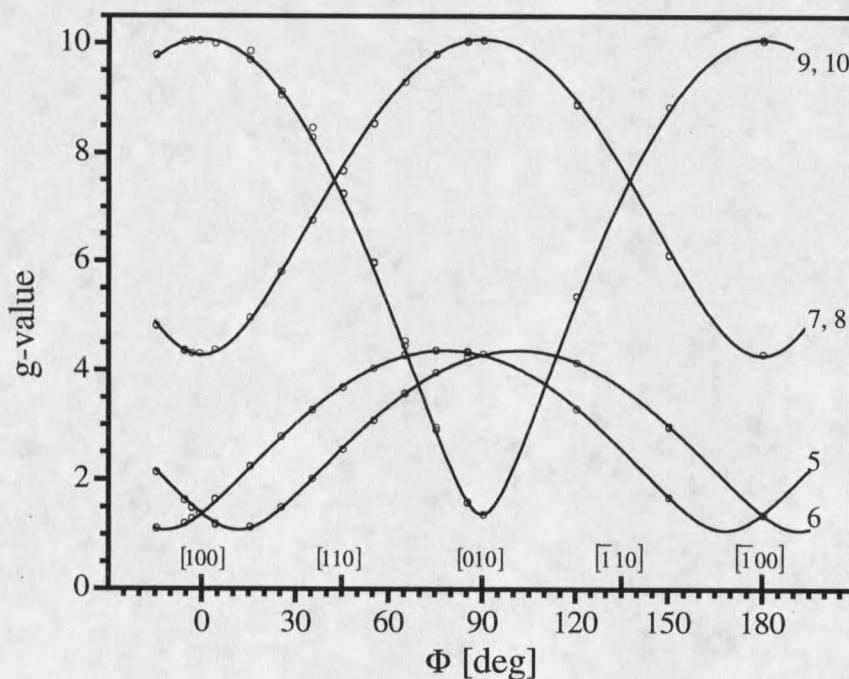


Figure 3.20. g-values for ${}^4I_{13/2}:Y_1$ with field in (001). Symbols (\circ) are data calculated from Zeeman spectra in Figure 3.15; solid curves are best fit. Site labels are inset.

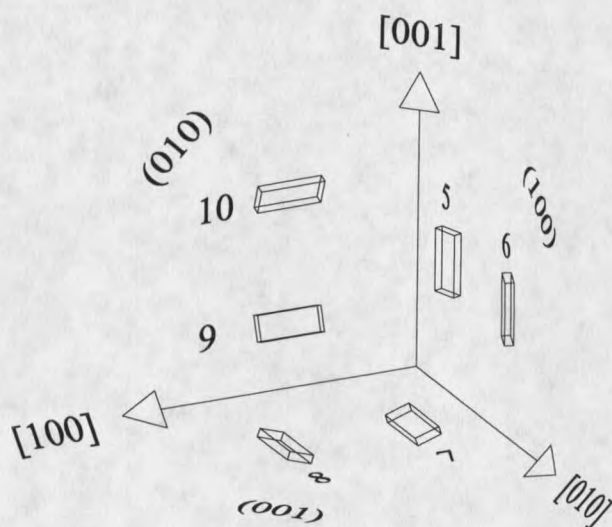


Figure 3.21. Graphical representation of ground state ${}^4I_{15/2}:Z_1$ g-tensors can be used to visualize g-value data in Figures 3.19 and 3.23. Zeeman splittings are proportional to the projection of the three dimensions of these “bricks” onto the applied magnetic field. Dimensions are to scale with principal g-values: ${}^s g_x = 1.603$, ${}^s g_y = 4.711$, ${}^s g_z = 11.93$; tipping angle is exaggerated to $+20^\circ$ for illustration: ${}^s \alpha = +2.06^\circ$.

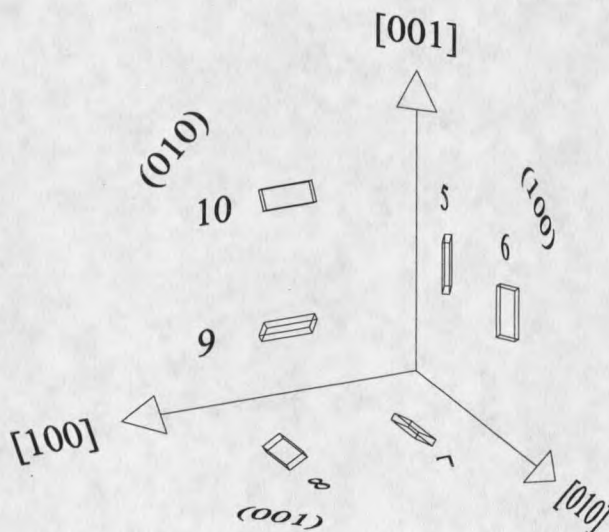


Figure 3.22. Graphical representation of excited state ${}^4I_{13/2}:Y_1$ g-tensors can be used to visualize g-value data in Figures 3.20 and 3.24. Zeeman splittings are proportional to the projection of the three dimensions of these “bricks” onto the applied magnetic field. Dimensions are to scale with principal g-values: ${}^s g_x = 1.08$, ${}^s g_y = 4.361$, ${}^s g_z = 10.07$; tipping angle in opposite sense compared to ground state and is exaggerated to -30° for illustration: ${}^s \alpha = -11.7^\circ$.

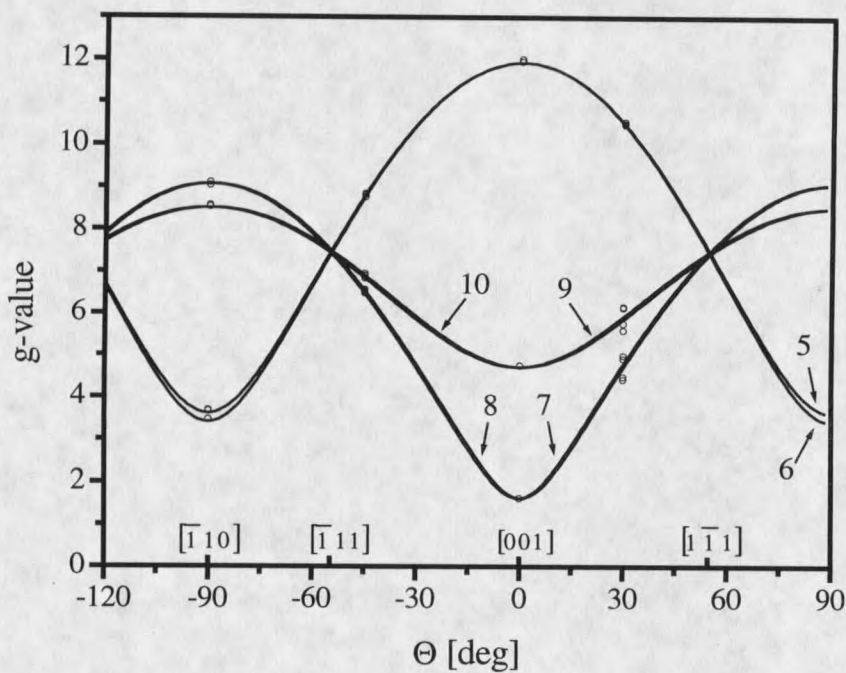


Figure 3.23. g-values for ${}^4I_{15/2}:Z_1$ with field in (110). Symbols (\circ) are data calculated from Zeeman spectra in Figure 3.15; solid curves are best fit. Site labels are inset.

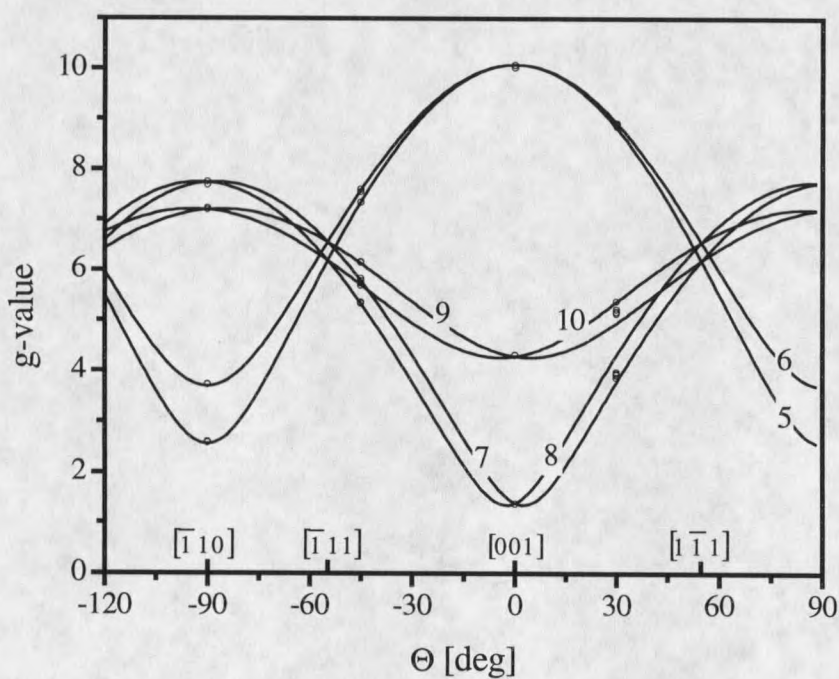


Figure 3.24. g-values for ${}^4I_{13/2}:Y_1$ with field in (110). Symbols (\circ) are data calculated from Zeeman spectra in Figure 3.15; solid curves are best fit. Site labels are inset.

Equations 3.4 were fit⁷⁸⁻⁸⁰ to the (001) plane g-values using $({}^s g_x, {}^s g_y, {}^s g_z; {}^s \alpha)$ and $({}^e g_x, {}^e g_y, {}^e g_z; {}^e \alpha)$ as fitting parameters. Table 3.2 presents best-fit \tilde{g} -tensor parameters and a collection of previously measured and calculated values.⁸¹ The average ratio between this work's ground state principal g-values and those of the previous EPR work is 0.969 ± 0.006 , a quite uniform discrepancy, which could be attributed to a 3% error in magnetic field calibration, as the SpectroMag magnetic field has not been calibrated since shipment from the manufacturer. The excited state principal g-values have not been previously measured. The tipping angle ${}^e \alpha$ is larger in magnitude and of the opposite sense with respect to the crystal axes compared with that for the ground state.

Table 3.2 also presents the g-values along $\langle 111 \rangle$, the interesting case alluded to previously. Two sets of ions, sites 5, 7, 9 and 6, 8, 10, each consisting of half of the C_2 ions are each orientationally equivalent with respect to $\langle 111 \rangle$ with eight transitions possible.

Table 3.2. Measured and calculated g-values for Er ³⁺ in C ₂ sites of Y ₂ O ₃						
⁴ I _{15/2} :Z ₁		^s g _x	^s g _y	^s g _z	^s g	^s α
Technique	Reference	[100]	[010]	[001]	⟨111⟩	
Optical Zeeman 0.005% Er ³⁺ :Y ₂ O ₃	This Work	1.603 ± 0.003	4.711 ± 0.006	11.93 ± 0.08	7.495 & 7.433	2.06 ± 0.06
EPR 0.01% Er ³⁺ :Y ₂ O ₃	58	1.645 ± 0.002	4.892 ± 0.005	12.314 ± 0.009	7.755 & 7.677	2.0 ± 0.2
FIR Spectroscopy Er ₂ O ₃	81	(0)	4.9	12.3		
Crystal Field Analysis	63	0.4	4.4	12.0	7.4	
Superposition Model Calculation	82	3.7	5.5	10.5	7.2	
Optical Zeeman Er ³⁺ :Y ₂ O ₃	61				7.5	
<hr/>						
⁴ I _{13/2} :Y ₁		^e g _x	^e g _y	^e g _z	^e g	^e α
Technique	Reference	[100]	[010]	[001]	⟨111⟩	
Optical Zeeman 0.005% Er ³⁺ :Y ₂ O ₃	This Work	1.08 ± 0.02	4.361 ± 0.003	10.07 ± 0.08	6.180 & 6.551	-11.7 ± 0.1

Discussion

The primary purpose of this work was to gain the necessary spectroscopic information to guide the choice of external magnetic field strength and orientation to optimize Er³⁺:Y₂O₃ for OCT devices by maximizing coherence lifetime. For this purpose it is useful to conceptually divide the Er³⁺ ions into two groups: "device ions" are those that contribute directly to generating the OCT signals; the remaining ions are

“environment ions” and contribute to dephasing of device ions through the fluctuating local fields they generate; device ions can dephase one another and in this context should be thought of as environment ions as well. Again, in the terminology of Mims the former are “A” ions and the latter are “B” ions.^{21,22} The two primary mechanisms⁵⁵ that reduce coherence lifetime of device ions at low temperatures and low magnetic fields in this host are direct process phonon scattering²⁶⁻³⁰ and electronic spin “flip-flop” transitions,^{21,22} these mechanisms depend on temperature and external magnetic field strength and orientation.

The relevant energy levels and transitions for direct phonon process dephasing of device ions in $\text{Er}^{3+}:\text{Y}_2\text{O}_3$ are presented in Figure 3.25. The optical transition for OCT devices is between the lower Zeeman components of the $^4I_{15/2}:\text{Z}_1$ ground and $^4I_{13/2}:\text{Y}_1$ excited states; the ground and excited doublet Zeeman splitting ΔE_g and ΔE_e are determined by the magnetic field strength and orientation. The direct process randomly drives device ions between two adjacent electronic states by resonant single phonon absorption and spontaneous phonon emission; in this case the two adjacent levels can be either the level of interest, the ground or excited state of the OCT device, and a nearby crystal field level, or the two Zeeman levels of the ground state or excited state. Lowering the temperature reduces the significance of direct phonon absorption process; by decreasing the available phonon energy and accessible density of states; at temperatures such that $k_B T \ll \Delta E_g$ (ΔE_e) the population of phonons resonant with the ground (excited) energy gap becomes vanishingly small and the direct process becomes negligible compared to other mechanisms.

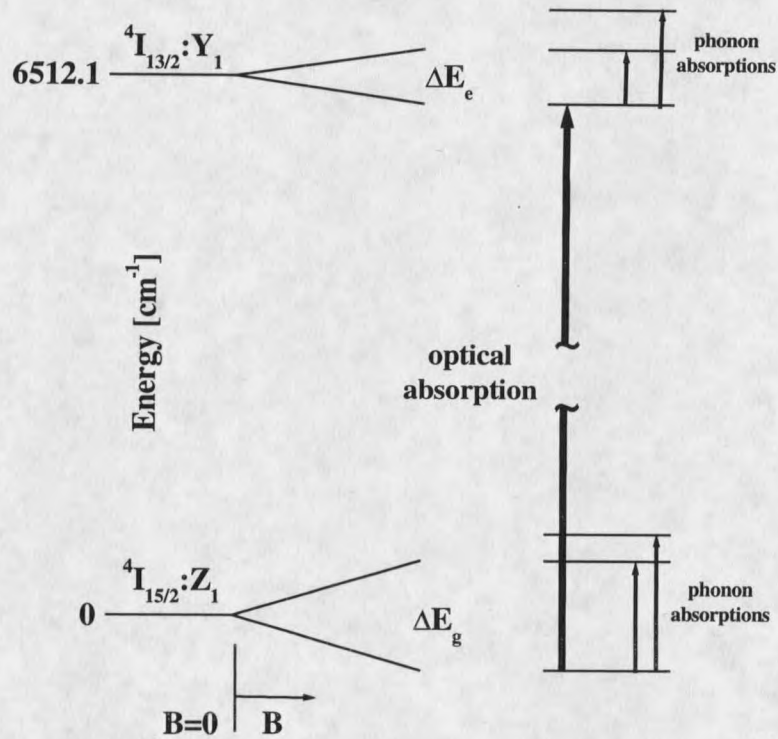


Figure 3.25. Relevant energy levels and transitions for direct phonon process dephasing. Phonon absorption from lower Zeeman components of ground and excited states to either upper Zeeman components or other nearby crystal field level causes dephasing at low temperatures.

The relevant energy levels and transitions for mutual “flip-flop” transition dephasing of device ions in $\text{Er}^{3+}:\text{Y}_2\text{O}_3$ are presented in Figure 3.26. Environment ion α is initially thermally promoted to the ground doublet upper Zeeman component as represented by the thick arrow at **1** and a nearby environment ion β is initially in the ground doublet lower Zeeman component represented by the thick arrow at **2**; under these conditions a nearby device ion has energy levels given by the heavy lines. Environment ion α spontaneously undergoes a spin “flip” to its lower Zeeman component given by the thin

arrow at **3** and resonantly drives environment ion β to spin “flop” to its upper Zeeman component given by the thin arrow at **4**; the mutual “flip-flop” conserves energy in the two-environment-ion system but changes the local magnetic field at the device ion and its new energy levels are given, for example, by the thin lines. Making the environment ion ground Zeeman splitting large compared to $k_B T$ freezes out mutual Er-Er flip-flop transitions by freezing out initial population of the upper level for environment ions.

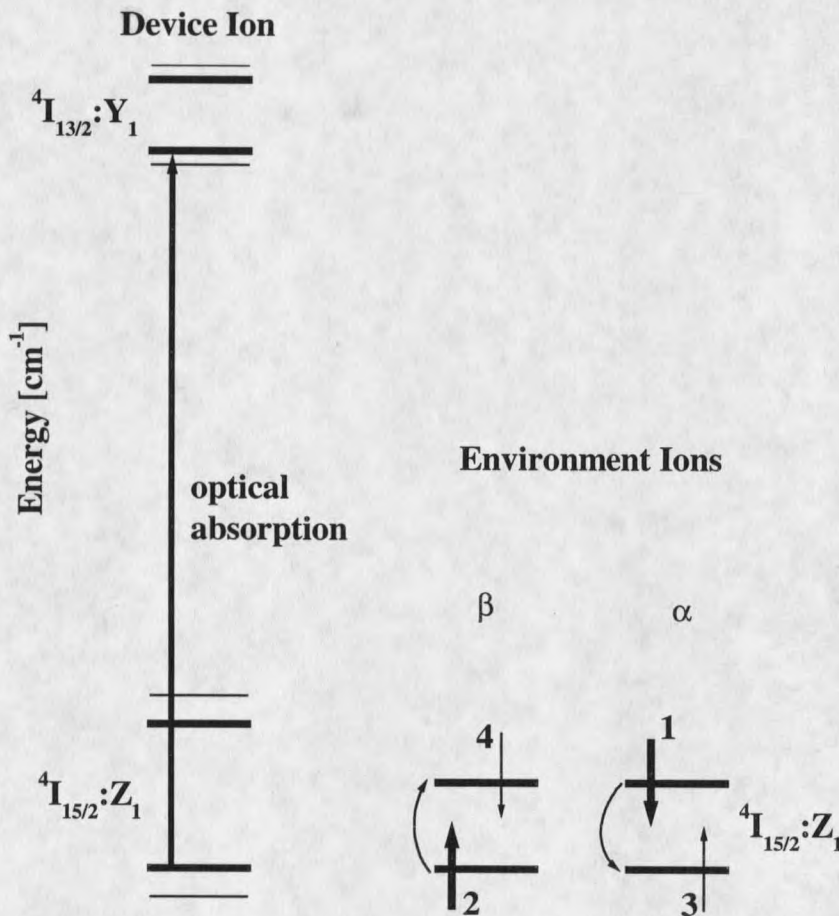


Figure 3.26. Relevant energy levels and transitions for spin flip-flop dephasing. Two environment ions undergo resonant energy conserving mutual flip-flop transition; resulting change of local magnetic field dephases device ion.

External magnetic field strength and direction determine device ion ground and excited Kramers doublet splittings, environment ion ground doublet splittings, and magnetic equivalence of orientationally inequivalent sites. Maximizing Zeeman splitting of the relevant doublets, by maximizing g-value, minimizes individual ion contributions to dephasing. Maximizing magnetic equivalence of ions utilized as device ions minimizes the overall doping necessary to achieve the desired overall absorption assuming the same oscillator strength, which maximizes average distance between ions, reducing mutual interaction. These optimization mechanisms, in a complicated system such as $\text{Er}^{3+}:\text{Y}_2\text{O}_3$, are often mutually incompatible. The orientation dependent Zeeman spectra and g-tensor data, along with published EPR data⁵⁸ for ions in C_{3i} sites, guide the tradeoffs surrounding choice of external magnetic field direction and magnitude needed to maximize coherence lifetime. Two external magnetic field directions that may optimize coherence lifetime are suggested by these data and they are discussed below along with their relative merits and drawbacks.

The most promising configuration orients the magnetic field along a $\langle 111 \rangle$ axis in a $\{110\}$ plane with a "b" transition energy of $\sigma = 6512.22 \text{ cm}^{-1}$ at $|\vec{B}| = 1.0 \text{ T}$. This is indicated in Figure 3.20 by I. Half of the ions in C_2 sites constitute the device ions and the other half contribute to the environment as a consequence of the two-fold inequivalence of C_2 sites for this orientation. The device ions have relatively large ground and excited g-values, 7.433 and 6.180, respectively and the C_2 site environment ions have a relatively large ground g-value, 7.495. The C_{3i} sites form two inequivalent groups in this orientation; one-fourth (three-fourths) of these environment ions have a

very high (moderate) ground g -value, 12.176 (5.124).⁵⁸ As the C_2 sites form two inequivalent groups in this orientation, each comprised of half of the sites, a relatively low overall doping is required and a high device-to-environment ion ratio (3/7) is obtained; a relatively low magnetic field is needed to depopulate the ground doublet upper component of the low g -value subset of ions in C_{3i} sites.

The second most favorable configuration orients the magnetic field near a $\langle 110 \rangle$ axis in a $\{001\}$ plane with a "b" transition energy of $\sigma = 6512.38 \text{ cm}^{-1}$ at $\vec{B} = 1.0 \text{ T}$ indicated in Figure 3.16 by II. While ions in sites labeled (7,8) are equivalent with respect to this plane and (9,10) are as well, they form two inequivalent sets at this orientation. Ground (excited) doublet g -values for ions in all four sites are 8.817 (7.494) at $\Phi = 42.84^\circ$ (42.43°), as shown in Figure 3.19 (3.20), and the b transitions are incidentally resonant, but are not magnetically equivalent at $\Phi \cong 44.5^\circ$ as shown in Figure 3.16. Two-thirds of the ions in C_2 sites constitute the device ions with very high ground and excited g -values; only one-third of the ions in C_2 sites contribute to the environment, but have low ground g -values (3.4 and 3.6). Ions in C_{3i} sites are inequivalent at this orientation and one-half of these environment ions have a very high ground g -value (10.1); however, the remaining half of these environment ions have a low ground g -value (3.3).⁵⁸ This orientation requires the lowest overall doping due to the large fraction of ions in C_2 sites utilized as device ions (2/3) and high device to environment ion ratio (2/3); a larger magnetic field is required however to depopulate the ground doublet upper component of the low g -value subsets of ions in C_2 and C_{3i}

sites. Table 3.3 summarizes the two interesting cases discussed above; both transitions were insensitive to laser polarization.

Table 3.3. Two magnetic field directions that hold promise for OCT devices.		
Orientation:	\vec{B} along $[\bar{1}11]$ in (110)	\vec{B} near $[110]$ in (001)
σ at $ \vec{B} = 1.0\text{T}$	6512.22 cm^{-1}	6512.38 cm^{-1}
Pros:	$\frac{1}{2}$ of C_2 ions used for device allowing lower overall doping for greater Er-Er average distance.	$\frac{2}{3}$ of C_2 ions used for device allowing lowest overall doping for greatest Er-Er average distance.
	Device ions have high ground and excited state g-values (7.433 and 6.180, respectively).	Device ions have high ground and excited state g-values (8.8 and 7.5).
	$\frac{1}{2}$ of C_2 ions contribute to environment.	Only $\frac{1}{3}$ of C_2 ions contribute to environment.
	C_2 environment ions have high ground state g-value (7.495).	$\frac{1}{2}$ of C_{3i} environment ions have high ground state g-value (10.1).
	$\frac{1}{4}$ of C_{3i} environment ions have high ground state g-value (12.176).	
Cons:	$\frac{3}{4}$ of C_{3i} environment ions have low ground state g-value (5.124).	Two-fold inequivalent C_2 environment ions have low ground state g-values (3.42 and 3.62).
		$\frac{1}{2}$ of C_{3i} environment ions have low ground state g-value (3.32).

The two orientations discussed above need further characterization to optimize $\text{Er}^{3+}:\text{Y}_2\text{O}_3$ for OCT correlators, memories and other devices. So far in this discussion other crystal field levels have been ignored, however, the Z_2 level of ions in C_{3i} sites may be significant as it lies only 10 cm^{-1} above Z_1 [Reference 64] and less than 2 Tesla

is necessary to split the Z_1 C_{3i} doublet by 10 cm^{-1} with the field along $[111]$. If the Z_2 level has comparable g -values the $Z_{1\uparrow}$ and $Z_{2\downarrow}$ levels may repel significantly, preventing the expected ground doublet splitting. Orientation dependent Zeeman investigations on the ions in C_{3i} sites are needed resolve this and are presently being conducted by G. Reinemer.

The knowledge gained in this study and the higher quality specimens of $\text{Er}^{3+}:\text{Y}_2\text{O}_3$ now available make possible further material characterization and device testing with crystals of known orientation and controlled absorption. Magnetic field and temperature dependence of the coherence lifetime and homogeneous linewidth should be characterized. Stimulated photon echo decays will establish storage lifetime of correlator patterns, operating conditions for other OCT devices, and provide further insight into dephasing mechanisms. Orientation dependent echo decays, needed to characterize the second orientation above, are also readily possible with the sample manipulator built for this work and described above.

CHAPTER 4

REAL-TIME ADDRESS-HEADER DECODER

Introduction

Real-time spatial-spectral holographic storage and processing of optical address headers has recently been proposed⁸³ and experimentally demonstrated.^{84,85} Those demonstrations were performed at the wavelengths of 580 and 793 nm employing Eu^{3+} and Tm^{3+} doped insulating crystals respectively. More recently, we have shown^{15,55} that erbium-doped insulating crystals, in particular $\text{Er}^{3+}:\text{Y}_2\text{SiO}_5$, have the required frequency-selective and coherence properties to provide operating wavelengths in the important 1550-nm telecommunication window. We report here our use of $\text{Er}^{3+}:\text{Y}_2\text{SiO}_5$ in a demonstration of address header decoding, one of several important components of high speed data routing by optical packet switching.^{3,83-85} The advantages of optical packet switching³ include fast data routing in the wavelength and space domains and transparency to packet bit rate and format. Specifically, we programmed a crystal to recognize binary-phase-shift key coded address headers and to decode an arbitrary sequence of these headers, resulting in spatially-discriminated optical output pulses. Each output pulse could be used to route or switch the optical data packet or the combined header and data packet in real-time.

